

Hybridizing anomalous Nernst effect in artificially tilted multilayer based on magnetic topological material

Takamasa Hirai^{1*}, Fuyuki Ando¹, Hossein Sepehri-Amin¹, and Ken-ichi Uchida^{1,2*}

¹*National Institute for Materials Science, Tsukuba, Ibaraki, Japan.*

²*Department of Advanced Materials Science, Graduate School of Frontier Sciences,
The University of Tokyo, Kashiwa, Chiba, Japan.*

*e-mail: HIRAI.Takamasa@nims.go.jp; UCHIDA.Kenichi@nims.go.jp

Transverse thermoelectric conversion holds significant potential in addressing complex challenges faced by classical Seebeck/Peltier modules. A promising transverse thermoelectric phenomenon is the anomalous Nernst effect (ANE) originating from nontrivial band structures in magnetic topological materials. However, the currently reported performance for ANE in topological materials, e.g., Co₂MnGa, remains insufficient for practical thermoelectric applications. Here, we unveil a new availability for ANE by integrating magnetic topological materials into artificially tilted multilayers (ATMLs), known to exhibit the structure-induced transverse thermoelectric conversion due to the off-diagonal Seebeck effect. Our experiments reveal that the transverse thermoelectric performance in Co₂MnGa-based ATMLs is improved through the hybrid action of ANE and the off-diagonal Seebeck effect, with the modulation of performance dependent on magnetization being significantly greater than the performance achievable with ANE alone. This unconventional synergy underscores the importance of hybrid transverse thermoelectric conversion and paves a way for advancing thermoelectric applications using magnetic materials.

Developments in thermoelectric technologies have garnered attention for their capability to directly convert a heat current \mathbf{J}_q into a charge current \mathbf{J}_c and vice versa, enabling power generation from wasted/environmental heat and solid-state refrigeration without mechanical moving parts¹⁻⁴. Conventional thermoelectric devices are based on the Seebeck effect and its Onsager reciprocal, that is, the Peltier effect, in which \mathbf{J}_c and \mathbf{J}_q flow in the same direction. Due to this longitudinal geometry, a thermoelectric module based on the Seebeck/Peltier effect usually consists of a bunch of *p*-type and *n*-type conductors connected electrically in series and thermally in parallel with many electrodes to enlarge the thermoelectric output. Although the Seebeck/Peltier module is progressing to the daily market, its complex three-dimensional structure remains indispensable problems, e.g., low mechanical endurance and energy loss due to many electrode junctions and their contact electrical and thermal resistances.

Transverse thermoelectric conversion has practical advantages over longitudinal thermoelectric effects⁴. The transverse thermoelectric effects allow interconversion between \mathbf{J}_c and \mathbf{J}_q in the orthogonal direction. Separating the \mathbf{J}_c and \mathbf{J}_q directions enables the enhancement of thermoelectric output simply by upscaling the size of a single thermoelectric material, which can reduce the number of electrodes and junctions in modules⁴. The ordinary Nernst effect (ONE) is a representative transverse thermoelectric effect; it is usually obtained in nonmagnetic conductors under an external magnetic field \mathbf{H} , referring to the generation of \mathbf{J}_c in the cross-product direction of the applied \mathbf{J}_q and \mathbf{H} owing to the Lorentz force. The ordinary Ettingshausen effect (OEE) is the Onsager reciprocal of ONE. In magnetic materials, the anomalous Nernst (Ettingshausen) effect manifests via the momentum-space Berry curvature related to the spin-orbit interaction and/or spin-dependent scattering acting on conduction carriers, where \mathbf{J}_c (\mathbf{J}_q) is generated in the cross-product direction of the applied \mathbf{J}_q (\mathbf{J}_c) and a spontaneous magnetization \mathbf{M} , which is referred to as ANE (AEE)^{5,6}. Unlike ONE/OEE, which requires a substantial magnitude of \mathbf{H} to generate a large transverse thermopower, ANE/AEE offers an advantage of operating at much smaller magnetic field values or in the absence of \mathbf{H} when magnetic materials have finite remanent magnetization. Such features and functionalities provided by ANE/AEE have motivated advanced research on spin caloritronics and condensed matter physics⁷⁻¹⁴. While ONE has been shown to scale with carrier mobility¹⁵, such simple scaling rules do not exist for ANE, and the material exploration for ANE is underway from various perspectives. By spotlighting the intrinsic Berry curvature contribution, several promising magnetic topological materials for transverse thermoelectrics have been discovered¹⁶⁻²⁵. However, the thermopower due to ANE is still $<8 \mu\text{V/K}$ and the record-high dimensionless figure of merit zT for ANE is approximately 7×10^{-4} at the temperature $T \sim 300 \text{ K}$ ²⁶, which is several orders of magnitude smaller than that for the Seebeck effect.

In this study, we provide a novel practical possibility for ANE/AEE in transverse thermoelectrics by hybridizing it into artificially tilted multilayers (ATMLs). The transverse thermoelectric conversion is not a unique feature of the Nernst/Ettingshausen effects but appears in anisotropic materials without requiring \mathbf{H} or \mathbf{M} . ATML is one example of such anisotropic materials and consists of alternately and obliquely stacked two different conductors²⁷⁻³⁶. The geometrically tilted structure generates finite off-diagonal components in the thermoelectric transport tensors owing to anisotropic carrier flows; thus, it is usually called the off-diagonal Seebeck/Peltier effect (ODSE/ODPE). Here, the sign of the thermoelectric output due to

ODSE/ODPE can be reversed by the 180° reversal of the relative angle between the tilting direction and input heat/charge current. Because the origin of ODSE/ODPE is the Seebeck/Peltier coefficients of constituent materials, a large transverse conversion by ODSE/ODPE has been realized using conventional thermoelectric materials^{27–36}. Herein, we report hybrid transverse magneto-thermoelectric conversion by superimposing ANE/AEE on ODSE/ODPE in ATMLs consisting of magnetic topological material/thermoelectric material stacks (Fig. 1). Although the hybrid transverse magneto-thermoelectric conversion based on ONE/OEE and ODSE/ODPE in ATMLs comprising nonmagnetic thermoelectric materials, i.e., Bi-Sb and Bi-Sb-Te, has recently been reported³⁷, hybridizing ANE/AEE and its feature superior to ONE/OEE has not been demonstrated and magnetic topological materials have not been incorporated into ATMLs so far. By means of the thermoelectric imaging technique based on lock-in thermography (LIT), we visualize the spatial distribution of transverse thermoelectric charge-to-heat current conversion processes in ATMLs based on a magnetic topological material and obtain large transverse thermoelectric cooling. Systematic LIT experiments separate the contribution of \mathbf{M} -dependent AEE from \mathbf{M} -independent ODPE, confirming the \mathbf{M} -induced tuning of transverse thermoelectric conversion by hybridizing ANE/AEE in the magnetic topological material. Thermopower measurements reveal that the ANE-induced modulation of zT for transverse thermoelectric conversion in ATMLs is several times larger than zT for ANE alone in single magnetic materials ever reported, owing to the existence of \mathbf{M} -independent ODSE. The development of ATML-based transverse magneto-thermoelectrics will boost research on thermoelectric device applications as well as topological materials science.

Results

Fabrication of Co₂MnGa-based artificially tilted multilayers

As the magnetic component of ATML, we selected a Weyl ferromagnet Co₂MnGa alloy, which is one of the magnetic topological materials and exhibits not only a top-level transverse thermopower due to ANE (6–8 $\mu\text{V/K}$) owing to its topological feature but also a relatively large negative Seebeck coefficient S_S (around $-30 \mu\text{V/K}$) among ferromagnetic conductors^{19,26,38–40}. The thermoelectric component of ATML was chosen from a viewpoint of improving ODSE/ODPE in ATML. Generally, a combination of two materials with large difference in S_S and with significantly different electrical and thermal conductivities (σ and κ , respectively) enhances the transverse thermoelectric performance for ODSE/ODPE in ATML^{29–37}. Thus, as the thermoelectric component of Co₂MnGa-based ATML, we mainly focused on p -type Bi_{0.2}Sb_{1.8}Te₃, which exhibits large positive S_S ($>100 \mu\text{V/K}$) and much smaller σ and κ than Co₂MnGa⁴¹.

To determine the structure of ATML, we analytically calculated transverse thermoelectric conversion performance of Co₂MnGa/Bi_{0.2}Sb_{1.8}Te₃ ATML through measuring the electrical, thermal, and thermoelectric transport properties of single Co₂MnGa and Bi_{0.2}Sb_{1.8}Te₃ alloys (see Methods). The transport properties of our polycrystalline Co₂MnGa and Bi_{0.2}Sb_{1.8}Te₃ alloys prepared by spark plasma sintering (SPS) are summarized in Supplementary Table 1. The σ and S_S values at a magnetic field of 0 T and 0.8 T are almost identical in Co₂MnGa and Bi_{0.2}Sb_{1.8}Te₃, indicating that the ordinary/anisotropic magnetoresistance and magneto-Seebeck effects are negligibly small in these materials below 0.8 T. The κ value of Co₂MnGa

is much larger than that of $\text{Bi}_{0.2}\text{Sb}_{1.8}\text{Te}_3$; such a large difference in κ makes it suitable for constructing ATMLs. Using σ , κ , and S_S values of the Co_2MnGa and $\text{Bi}_{0.2}\text{Sb}_{1.8}\text{Te}_3$ slabs, the electrical and thermal conductivities orthogonal to each other (σ_{xx} and κ_{yy}) and the transverse thermopower due to ODSE (S_{OD}) were simulated for $\text{Co}_2\text{MnGa}/\text{Bi}_{0.2}\text{Sb}_{1.8}\text{Te}_3$ ATML, according to the equations in ref. 36 (see Supplementary Note 1). Figure 2a-d respectively display the contour maps for S_{OD} , σ_{xx} , κ_{yy} , and zT for simulated ODSE, $z_{\text{OD}}T$ ($= S_{\text{OD}}^2 \sigma_{xx} T / \kappa_{yy}$), in $\text{Co}_2\text{MnGa}/\text{Bi}_{0.2}\text{Sb}_{1.8}\text{Te}_3$ ATML as functions of a tile angle θ and thickness ratio $R = t_{\text{M}} / (t_{\text{TE}} + t_{\text{M}})$ at the zero magnetic field, where $t_{\text{M(TE)}}$ is the thickness of magnetic (thermoelectric) layer and $T = 300$ K was used. Here, it is found that the values of $\theta \sim 30^\circ$ and $R \sim 0.5$ in $\text{Co}_2\text{MnGa}/\text{Bi}_{0.2}\text{Sb}_{1.8}\text{Te}_3$ ATML satisfy the optimal $z_{\text{OD}}T$ (~ 0.13), which is much larger than zT for ANE in single-magnetic materials.

Based on the above simulation, Co_2MnGa -based ATML was prepared by following procedures (see also Methods). Initially, we prepared a cylindrical Co_2MnGa slab with a diameter of 20 mm through the SPS method, subsequently slicing it into several disks each with t_{M} of 0.75 mm. Then, these sliced Co_2MnGa discs and Bi-Sb-Te powders were alternately piled up and bonded together via SPS. Notably, the Bi-Sb-Te powder used here is identical to that utilized in sintering the single $\text{Bi}_{0.2}\text{Sb}_{1.8}\text{Te}_3$ slab. Here, we confirmed that the sharp repeating boundaries in the $\text{Co}_2\text{MnGa}/\text{Bi}_{0.2}\text{Sb}_{1.8}\text{Te}_3$ stack through structural characterizations; the composition of the bulk regions of each layer was uniform and the atomic interdiffusion was limited to a region of ~ 10 μm at the $\text{Co}_2\text{MnGa}/\text{Bi}_{0.2}\text{Sb}_{1.8}\text{Te}_3$ interfaces (Supplementary Fig. 1). Finally, the $\text{Co}_2\text{MnGa}/\text{Bi}_{0.2}\text{Sb}_{1.8}\text{Te}_3$ stacks were cut into a rectangular slab with a size of $\sim 15 \times 2 \times 2$ mm^3 and $\theta \sim 30^\circ$. Through microscopic analysis, we estimated the t_{TE} value of our $\text{Co}_2\text{MnGa}/\text{Bi}_{0.2}\text{Sb}_{1.8}\text{Te}_3$ ATML to be 1.0 mm, resulting in the R value of 0.43. This confirms the fabrication of $\text{Co}_2\text{MnGa}/\text{Bi}_{0.2}\text{Sb}_{1.8}\text{Te}_3$ ATML with the θ and R values close to the optimal conditions for $z_{\text{OD}}T$, as depicted in Fig. 2d.

To check the thermoelectric transport property in our polycrystalline Co_2MnGa , we measured ANE using the plain Co_2MnGa slab (Supplementary Fig. 2). The anomalous Nernst coefficient of our Co_2MnGa is estimated to be 6.9 $\mu\text{V}/\text{K}$, which is comparable to the values in bulk single-crystalline Co_2MnGa ^{19,38} as well as polycrystalline Co_2MnGa ^{40,42}. The σ (κ) value of our polycrystalline Co_2MnGa is almost same as (smaller than) that of single-crystalline Co_2MnGa ³⁸.

Lock-in thermography measurement

To investigate the transverse thermoelectric conversion processes in our ATML, LIT measurements were conducted (see Methods). The LIT technique based on the infrared thermometry enables the visualization of the temporal response and spatial distribution of temperature changes induced by an external periodic input with high temperature (< 0.1 mK) and spatial (around 10-20 μm) resolutions⁴³. In LIT measurements, heating or cooling signals harmonically oscillating at the frequency of the periodic input signal are extracted as thermal images^{37,44-48}. In this study, a square-wave-modulated charge current with the frequency f ($= 0.2$ -10.0 Hz), amplitude J_c ($= 1$ A), and zero offset was applied to the sample along its longitudinal direction (x -axis in Fig. 3a,i), which induces temperature changes due to the thermoelectric conversion as well as Joule heating. By extracting the first harmonic component of the thermal images, the contribution of the thermoelectric effects ($\propto J_c$) can be retrieved free from that of Joule heating ($\propto J_c^2$)^{46,47}. The captured thermal

images were transformed into lock-in amplitude A and phase ϕ images through Fourier analysis, where the A (ϕ) image shows the distribution of the magnitude (sign) of the induced temperature modulation and the ϕ image also gives information on the time delay of the temperature modulation due to thermal diffusion. We carried out the LIT measurements in two configurations: cross-section (Fig. 3a) and top-side configurations (Fig. 3i).

Visualization of off-diagonal Peltier effect in Co₂MnGa-based artificially tilted multilayer

Figure 3 shows the results of the LIT measurements for Co₂MnGa/Bi_{0.2}Sb_{1.8}Te₃ ATML in the absence of \mathbf{H} . First, we examine the results for the cross-section configuration (Fig. 3a-h). The A and ϕ images at $f = 10.0$ Hz (top panels) and 0.2 Hz (bottom panels) are displayed in Fig. 3c and 3d, respectively. We can obtain information on the transient (nearly steady-state) temperature distribution induced by thermoelectric effects at $f = 10.0$ Hz (0.2 Hz)^{37,46}. At $f = 10.0$ Hz, temperature modulation signals are obtained in the vicinity of the interfaces between the Co₂MnGa and Bi_{0.2}Sb_{1.8}Te₃ layers; the A value reaches a maximum at the oblique junction interfaces and the 180° reversal of ϕ between the neighboring interfaces appears due to the Peltier effect. Importantly, in contrast to a Peltier-effect-induced temperature modulation at non-oblique junction interfaces^{49,50}, the A signal is non-uniform along the oblique interfaces owing to the non-uniform \mathbf{J}_c flow in ATML, which is the origin of the transverse thermoelectric conversion stemming from ODPE. At $f = 0.2$ Hz, the cooling/heating signals are broadened through thermal diffusion, and the A and ϕ signals exhibit zigzag-shaped patterns with an angle corresponding to a θ value of $\sim 30^\circ$. As shown in the bottom panel of Fig. 3d, the ϕ value at the upper (lower) edge of the sample presents almost uniform values of $\sim 180^\circ$ ($\sim 0^\circ$) (see also the x -directional line profile shown in Fig. 3f), confirming transverse thermoelectric cooling and heating due to ODPE in Co₂MnGa/Bi_{0.2}Sb_{1.8}Te₃ ATML. Note that the A value periodically changes along the x direction because of the multilayer structure (Fig. 3e). The transverse thermoelectric cooling behavior can be clearly identified in the top-side configuration (Fig. 3i-n).

To evaluate the transverse thermoelectric cooling/heating performance of Co₂MnGa/Bi_{0.2}Sb_{1.8}Te₃ ATML, we averaged the LIT results over one Co₂MnGa/Bi_{0.2}Sb_{1.8}Te₃ unit. Figure 3g,h (3o,p) shows the f dependence of the averaged A and ϕ values, A_{ave} and ϕ_{ave} , for one Co₂MnGa/Bi_{0.2}Sb_{1.8}Te₃ unit in the cross-section (top-side) configuration, where the averaged areas are defined in Fig. 3c,d (Fig. 3k,l). In both configurations, the A_{ave} value monotonically increases and the ϕ_{ave} value gradually gets closer to 180° with decreasing f , that is, approaching the temperature distribution in the steady state. The observed transverse thermoelectric temperature modulation is ~ 1 K at $f = 0.2$ Hz, which is much larger than that generated only by using OEE or AEE in a single conductor in a similar experimental condition^{11,12,51}.

Transverse magneto-thermoelectric conversion in Co₂MnGa-based artificially tilted multilayer

Next, we investigate the temperature modulation induced by transverse magneto-thermoelectric effects in Co₂MnGa/Bi_{0.2}Sb_{1.8}Te₃ ATML from the LIT images captured under an application of \mathbf{H} with the magnitude of H . To hybridize ODPE and AEE, \mathbf{H} was applied along the vertical direction (z axis in Fig. 3a) [horizontal short direction (y axis in Fig. 3i)] of the sample in the cross-section (top-side) configuration using

electromagnets. The temperature change arising from the transverse magneto-thermoelectric effects, namely, AEE and/or OEE, exhibits an antisymmetric dependence with respect to the \mathbf{H} direction, whereas the temperature change due to ODPE and/or the ordinary/anisotropic magneto-Peltier effect showcases a symmetric dependence (note again that the contribution of the ordinary/anisotropic magneto-Peltier effect, the Onsager reciprocal of the ordinary/anisotropic magneto-Seebeck effect, is negligible in our samples). Thus, we calculate H -odd-dependent LIT signals using the following equations:

$$A_{\text{odd}} = |A(+H)e^{-i\phi(+H)} - A(-H)e^{-i\phi(-H)}|/2 \quad (1)$$

$$\phi_{\text{odd}} = -\arg[A(+H)e^{-i\phi(+H)} - A(-H)e^{-i\phi(-H)}], \quad (2)$$

where $A(+H)$ [$\phi(+H)$] and $A(-H)$ [$\phi(-H)$] are defined as A (ϕ) measured in the positive ($-z$ or $+y$ direction) and negative ($+z$ or $-y$ direction) H , respectively. Figure 4a,b shows the A_{odd} and ϕ_{odd} images for $\text{Co}_2\text{MnGa}/\text{Bi}_{0.2}\text{Sb}_{1.8}\text{Te}_3$ ATML at $\mu_0|H| = 0.8$ T and $f = 10.0$ Hz (top panels) and 0.2 Hz (bottom panels) in the cross-section configuration, where μ_0 represents the vacuum permeability. The distribution of the A_{odd} and ϕ_{odd} signals inside ATML is obviously different from that arising from ODPE at zero magnetic field (Fig. 3c,d). As highlighted in the images at $f = 10.0$ Hz, the A_{odd} and ϕ_{odd} signals appear in the Co_2MnGa regions. Importantly, despite their different distributions, the H -odd-dependent components contribute to the transverse thermoelectric cooling/heating with the same symmetry as ODPE (compare the thermal images at $f = 0.2$ Hz in Figs. 3d and 4b). Hereafter, we focus on the results for the top-side configuration because the signals at the sample edges in the cross-section configuration are difficult to use for quantitative discussions due to the limitation of spatial resolution of LIT³⁷. Figure 5a,b shows the A_{odd} and ϕ_{odd} images for $\text{Co}_2\text{MnGa}/\text{Bi}_{0.2}\text{Sb}_{1.8}\text{Te}_3$ ATML at $\mu_0|H| = 0.8$ T and $f = 10.0$ Hz and 0.2 Hz in the top-side configuration. At $f = 10.0$ Hz, the A_{odd} signals in the Co_2MnGa regions are greater than those in the $\text{Bi}_{0.2}\text{Sb}_{1.8}\text{Te}_3$ regions and the ϕ_{odd} signals are reversed between the Co_2MnGa ($\sim 0^\circ$) and $\text{Bi}_{0.2}\text{Sb}_{1.8}\text{Te}_3$ ($\sim 180^\circ$) regions. As shown in Fig. 5c,d, in the $\mu_0|H|$ range of 0.2 - 1.0 T, the A_{odd} value is almost constant in the Co_2MnGa region with $\phi_{\text{odd}} \sim 0^\circ$, while the A_{odd} value linearly increases with increasing H in the $\text{Bi}_{0.2}\text{Sb}_{1.8}\text{Te}_3$ region with $\phi_{\text{odd}} \sim 180^\circ$. These tendencies are consistent with the H dependence of the ANE signal in Co_2MnGa and that of the ONE signal in $\text{Bi}_{0.2}\text{Sb}_{1.8}\text{Te}_3$ (Supplementary Fig. 2), indicating that the A and ϕ images measured at non-zero H contain the contributions of AEE in Co_2MnGa as well as OEE in $\text{Bi}_{0.2}\text{Sb}_{1.8}\text{Te}_3$. At lower f , the LIT images exhibit different temperature distributions as a result of superimposed contributions of AEE and OEE through thermal diffusion; the almost uniform ϕ_{odd} signal ($\sim 0^\circ$) across the entire sample area is observed at $f = 0.2$ Hz with the enhanced A_{odd} signal. Figure 5e,f shows the f dependence of the A_{odd} and ϕ_{odd} values in the Co_2MnGa and $\text{Bi}_{0.2}\text{Sb}_{1.8}\text{Te}_3$ regions, respectively. With approaching the steady state, the A_{odd} value monotonically increases in both the Co_2MnGa and $\text{Bi}_{0.2}\text{Sb}_{1.8}\text{Te}_3$ regions (Fig. 5e), while the ϕ_{odd} value remains $\sim 0^\circ$ in the Co_2MnGa region and gradually changes from $\sim 180^\circ$ to $\sim 0^\circ$ in the $\text{Bi}_{0.2}\text{Sb}_{1.8}\text{Te}_3$ region (Fig. 5f). These results indicate that the AEE-induced \mathbf{J}_q from the Co_2MnGa layer predominantly affects the temperature change even on the $\text{Bi}_{0.2}\text{Sb}_{1.8}\text{Te}_3$ surface, suggesting that ANE/AEE in Co_2MnGa modulates the transverse thermoelectric conversion in $\text{Co}_2\text{MnGa}/\text{Bi}_{0.2}\text{Sb}_{1.8}\text{Te}_3$ ATML in the steady state.

To verify our interpretation that the A_{odd} and ϕ_{odd} signals stem from ANE in Co_2MnGa , we must distinguish the ANE contribution from the Seebeck-effect-driven anomalous Hall effect (AHE) observed in magnetic/thermoelectric hybrid systems^{40,52,53}, which can superimpose additional transverse thermopower onto ANE via the combination of the Seebeck effect in thermoelectric layers and AHE in magnetic layers. To this end, we performed the same LIT measurements for $\text{Co}_2\text{MnGa}/\text{Bi}_2\text{Te}_3$ ATML, in which p -type $\text{Bi}_{0.2}\text{Sb}_{1.8}\text{Te}_3$ was replaced by n -type Bi_2Te_3 . Here, the sign of the contribution of Seebeck-effect-driven AHE should be reversed due to the different sign of S_S between $\text{Bi}_{0.2}\text{Sb}_{1.8}\text{Te}_3$ and Bi_2Te_3 . The fabrication procedure of ATML and the optimization conditions of ODSE for $\text{Co}_2\text{MnGa}/\text{Bi}_2\text{Te}_3$ ATML are the same as those for $\text{Co}_2\text{MnGa}/\text{Bi}_{0.2}\text{Sb}_{1.8}\text{Te}_3$ ATML (Methods and Supplementary Fig. 3). The results of the LIT measurements for $\text{Co}_2\text{MnGa}/\text{Bi}_2\text{Te}_3$ ATML are summarized in Supplementary Figs. 4-6. The direction of ODPE-induced \mathbf{J}_q is opposite and the magnitude of temperature modulation decreases, compared with that of $\text{Co}_2\text{MnGa}/\text{Bi}_{0.2}\text{Sb}_{1.8}\text{Te}_3$ ATML. This is because the sign (magnitude) of the difference in the Peltier coefficient ($= S_S T$) between the magnetic and thermoelectric components of ATMLs, $\Delta S_S T$ with ΔS_S being the difference in S_S , was reversed (reduced) by changing the sign of S_S of the thermoelectric component from positive to negative. On the other hand, the H -odd component of the LIT signals in $\text{Co}_2\text{MnGa}/\text{Bi}_2\text{Te}_3$ ATML is comparable to that in $\text{Co}_2\text{MnGa}/\text{Bi}_{0.2}\text{Sb}_{1.8}\text{Te}_3$ ATML because of almost identical thermopower due to ONE between $\text{Bi}_{0.2}\text{Sb}_{1.8}\text{Te}_3$ and Bi_2Te_3 (Supplementary Table 1 and Fig. 2). Since the sign of the transverse thermopower due to ANE in Co_2MnGa and Seebeck-effect-driven AHE in bilayers consisting of Co_2MnGa and n -type (p -type) thermoelectric materials is the same (opposite)^{53,54}, the transverse magneto-thermoelectric conversion in $\text{Co}_2\text{MnGa}/\text{Bi}_2\text{Te}_3$ ATML should be improved over that in $\text{Co}_2\text{MnGa}/\text{Bi}_{0.2}\text{Sb}_{1.8}\text{Te}_3$ ATML if Seebeck-effect-driven AHE contributes effectively to ATMLs. However, the observed A_{odd} value in the Co_2MnGa region of $\text{Co}_2\text{MnGa}/\text{Bi}_2\text{Te}_3$ ATML is slightly smaller than that of $\text{Co}_2\text{MnGa}/\text{Bi}_{0.2}\text{Sb}_{1.8}\text{Te}_3$ ATML, which could be explained by electrical shunting in $\text{Bi}_{0.2}\text{Sb}_{1.8}\text{Te}_3$ and Bi_2Te_3 . These results indicate that the contribution of Seebeck-effect-driven AHE on the total transverse magneto-thermopower is much smaller than that of ANE in our samples due to the unoptimized θ value and size ratio of the magnetic and thermoelectric layers for the magneto-thermoelectric effects (note that θ in our samples is designed for ODSE).

Hybrid transverse magneto-thermoelectric conversion

Here, we discuss the ANE-induced modulation of the total transverse thermoelectric conversion in our Co_2MnGa -based ATMLs. From an application viewpoint, the performance of the temperature modulation in the steady state is important; therefore, we focused on the results at the minimum f ($= 0.2$ Hz). Figure 6a,b displays the H dependence of the A_{ave} and ϕ_{ave} signals at $f = 0.2$ Hz for $\text{Co}_2\text{MnGa}/\text{Bi}_{0.2}\text{Sb}_{1.8}\text{Te}_3$ and $\text{Co}_2\text{MnGa}/\text{Bi}_2\text{Te}_3$ ATMLs in the top-side configuration. In both ATMLs, the magnitude of A_{ave} exhibits the clear asymmetric H dependence with a saturation behavior, which is consistent with the magnetization curve of Co_2MnGa in ATMLs (displayed in Fig. 6a,b), owing to the AEE contribution. Because of the dominant ODPE contribution and the positive (negative) ΔS_S for $\text{Co}_2\text{MnGa}/\text{Bi}_{0.2}\text{Sb}_{1.8}\text{Te}_3$ ($\text{Co}_2\text{MnGa}/\text{Bi}_2\text{Te}_3$) ATML, an H -independent ϕ_{ave} value of $\sim 180^\circ$ ($\sim 0^\circ$) appears in $\text{Co}_2\text{MnGa}/\text{Bi}_{0.2}\text{Sb}_{1.8}\text{Te}_3$ ($\text{Co}_2\text{MnGa}/\text{Bi}_2\text{Te}_3$) ATML.

The A_{ave} value is enhanced by applying the negative (positive) H in $\text{Co}_2\text{MnGa}/\text{Bi}_{0.2}\text{Sb}_{1.8}\text{Te}_3$ ($\text{Co}_2\text{MnGa}/\text{Bi}_2\text{Te}_3$) ATML because the direction of generated \mathbf{J}_q due to ODPE at zero H is opposite to (the same as) that due to AEE at the positive H . The H -induced modulation ratio of the temperature change for $\text{Co}_2\text{MnGa}/\text{Bi}_{0.2}\text{Sb}_{1.8}\text{Te}_3$ and $\text{Co}_2\text{MnGa}/\text{Bi}_2\text{Te}_3$ ATMLs is estimated to be $|A_{\text{ave}}(+H) - A_{\text{ave}}(-H)|/A_{\text{ave}}(0 \text{ T}) \sim 5\%$ and 15% at $\mu_0|H| > 0.2 \text{ T}$, respectively. The larger H -induced modulation ratio for $\text{Co}_2\text{MnGa}/\text{Bi}_2\text{Te}_3$ ATML is due to the smaller ODPE contribution [$= A_{\text{ave}}(0 \text{ T})$]. These results reveal that AEE can exert a clear change in the average temperature modulation in ATMLs, although AEE appears only in the Co_2MnGa layers.

To quantitatively evaluate the thermoelectric performance based on the hybrid action of ODSE and ANE, we measured the transverse thermopower by applying a temperature difference ΔT between the top and bottom surfaces of Co_2MnGa -based ATMLs (see also Methods). Figure 7a,b shows the H dependence of the transverse thermoelectric voltage V_T at various values of ΔT for $\text{Co}_2\text{MnGa}/\text{Bi}_{0.2}\text{Sb}_{1.8}\text{Te}_3$ and $\text{Co}_2\text{MnGa}/\text{Bi}_2\text{Te}_3$ ATMLs, respectively. With increasing ΔT , both the offset thermoelectric voltage due to ODSE and the H -induced change in the thermoelectric voltage due to ANE increase. Here, only the sign of the ODSE contribution is reversed between $\text{Co}_2\text{MnGa}/\text{Bi}_{0.2}\text{Sb}_{1.8}\text{Te}_3$ and $\text{Co}_2\text{MnGa}/\text{Bi}_2\text{Te}_3$ ATMLs because of the sign reversal of ΔS_s . Figure 7c shows the temperature gradient ∇T dependence of the transverse thermoelectric field E_T at $\mu_0 H = \pm 0.8 \text{ T}$. The application of H clearly changes the slope of the E_T - ∇T plots, i.e., the transverse thermopower S_T ; the negative (positive) H application enhances the magnitude of S_T of $\text{Co}_2\text{MnGa}/\text{Bi}_{0.2}\text{Sb}_{1.8}\text{Te}_3$ ($\text{Co}_2\text{MnGa}/\text{Bi}_2\text{Te}_3$) ATML.

By combining the measured S_T values and simulated σ_{xx} and κ_{yy} values (Fig. 2b,c and caption in Fig. 7), we estimate the figure of merit for hybrid transverse magneto-thermoelectric conversion $z_T T$ ($= S_T^2 \sigma_{xx} T / \kappa_{yy}$) at $T = 300 \text{ K}$ to be 0.088 and 0.095 (0.010 and 0.008) at $+0.8$ and -0.8 T , respectively, for $\text{Co}_2\text{MnGa}/\text{Bi}_{0.2}\text{Sb}_{1.8}\text{Te}_3$ ($\text{Co}_2\text{MnGa}/\text{Bi}_2\text{Te}_3$) ATML. These $z_T T$ values are several orders of magnitude larger than zT for ANE, $z_N T$, in single magnetic materials ($< 7 \times 10^{-4}$ at 300 K). Most importantly, in our Co_2MnGa -based ATMLs, especially $\text{Co}_2\text{MnGa}/\text{Bi}_{0.2}\text{Sb}_{1.8}\text{Te}_3$ ATML, the \mathbf{M} -dependent change in $z_T T$ is also several times larger than $z_N T$. The reason why we achieve such a significant transverse magneto-thermoelectric modulation, surpassing the record-high $z_N T$, is owing to the presence of \mathbf{M} -independent ODSE. Since the zT value is proportional to the square of the thermopower, $z_N T$ and $z_T T$ satisfy the following relations:

$$z_N T \propto S_N^2 \quad (3)$$

$$z_T T \propto S_T^2 = (S_{\text{OD}} + \tilde{S}_N)^2 = S_{\text{OD}}^2 + 2S_{\text{OD}}\tilde{S}_N + \tilde{S}_N^2, \quad (4)$$

where \tilde{S}_N is the effective anomalous Nernst coefficient considering the reduction due to the superimposition of ONE and the shunting effect in ATMLs. In ATMLs, the ANE contribution for $z_T T$ produces the additional $2S_{\text{OD}}\tilde{S}_N$ term of which magnitude depends on both S_N and S_{OD} (i.e., S_T at $\mu_0 H = 0 \text{ T}$), resulting that the magneto-thermoelectric modulation of $z_T T$ gets much greater than $z_N T$ owing to larger $|S_{\text{OD}}|$ than $|S_N|$. In fact, such a hybridization of ODSE and ANE is more prominent in $\text{Co}_2\text{MnGa}/\text{Bi}_{0.2}\text{Sb}_{1.8}\text{Te}_3$ ATML ($S_{\text{OD}} = -56.1 \mu\text{V/K}$) than in $\text{Co}_2\text{MnGa}/\text{Bi}_2\text{Te}_3$ ATMLs ($S_{\text{OD}} = +17.2 \mu\text{V/K}$). Thus, this unconventional synergy offers another route to develop physics and materials science on ANE.

Discussion

Finally, we discuss prospects for advancing the ANE-hybridized transverse magneto-thermoelectric conversion in ATMLs. Exploring a magnetic material showing large S_N , which is the current mainstream research in spin caloritronics and topological materials science, is properly significant. If one can develop a material that exhibits twice larger S_N than Co_2MnGa , for example, by introducing it in place of Co_2MnGa in $\text{Co}_2\text{MnGa}/\text{Bi}_{0.2}\text{Sb}_{1.8}\text{Te}_3$ ATML, the ANE-induced modulation of $z_T T$ reaches 0.01 at room temperature. In addition to ANE, the large magnitude of the base transverse thermopower at zero field due to ODSE is also indispensable, according to the results shown in the last section; a superior ODSE performance, e.g., larger ΔS_S in ATMLs, can enhance the magneto-thermoelectric modulation even if the contribution of ANE alone is the same. Supplementary Fig. 7a shows the dependence of the absolute value of \tilde{S}_N on the magneto-thermoelectric modulation of $z_T T$, i.e., $\Delta(z_T T) = \tilde{S}_N^2 + 2|S_{\text{OD}}\tilde{S}_N|$, at various magnitudes of S_{OD} . The presence of ODSE not only significantly improves the $\Delta(z_T T)$ value without changing $|\tilde{S}_N|$ but also further increases the contribution of ANE on $\Delta(z_T T)$, i.e., the slope in Supplementary Fig. 7a, resulting in $\Delta(z_T T) \sim 0.05$ (~ 0.13) at $|\tilde{S}_N| = 7 \mu\text{V/K}$ ($20 \mu\text{V/K}$) and $|S_{\text{OD}}| = 100 \mu\text{V/K}$ at room temperature (note that over $100 \mu\text{V/K}$ of $|S_{\text{OD}}|$ has been reported in many ATMLs in previous studies^{32–35,37}). Furthermore, as shown in Supplementary Fig. 7b, improving both \tilde{S}_N and S_{OD} can enhance the $z_T T$ value, e.g., $z_T T \sim 0.35$ at $|\tilde{S}_N| = 7 \mu\text{V/K}$ and $|S_{\text{OD}}| = 100 \mu\text{V/K}$ at room temperature. These findings emphasize the importance of investigating both ANE and ODSE (i.e., S_N and S_S), which have been studied independently. Especially, the exploration of magnetic materials with large S_S has received little attention so far, leading to new research on magnetic materials. Interface engineering in ATMLs is also promising since multilayering could increase S_N itself intentionally via an interfacial spin-orbit interaction⁵⁵. Further superimposition of the contribution of magneto-thermoelectric effects other than ANE is another route for improving the performance of transverse thermoelectric conversion in ATMLs. Since this study focuses on the demonstration of hybridizing ANE in ATMLs using a magnetic topological material, the contribution of ONE was not optimized; the opposite sign of S_N in $\text{Bi}_{0.2}\text{Sb}_{1.8}\text{Te}_3$ or Bi_2Te_3 against S_N in Co_2MnGa decreases the magneto-thermoelectric modulation. Optimizing the θ value and size ratio of magnetic and thermoelectric layers is also effective for further manifesting the contribution of Seebeck-effect-driven AHE in ATMLs. By appropriately designing these factors and including ODSE, ANE, ONE, Seebeck-effect-driven AHE, and other magneto-thermoelectric effects, dramatic improvements in the transverse magneto-thermoelectric conversion performance are possible in ATMLs.

In summary, we have demonstrated the giant ANE-induced modulation of transverse thermoelectric conversion that far exceeds the performance of ANE alone by fabricating ATMLs using a Weyl ferromagnet Co_2MnGa and thermoelectric materials. The infrared imaging technique based on LIT visualized the current-induced transverse thermoelectric cooling/heating behaviors. The LIT measurements under various H values clarified the contributions of structure-induced ODPE, \mathbf{H} -induced OEE, and \mathbf{M} -induced AEE in Co_2MnGa -based ATMLs, proving the modulation of the transverse thermoelectric conversion performance due to hybridization of ODSE and ANE in Co_2MnGa . Owing to the existence of ODSE, the magneto-thermoelectric

modulation of $z_T T$ in Co_2MnGa -based ATMLs induced by ANE was much greater than $z_N T$ in a single Co_2MnGa alloy that exhibits the record-high ANE performance at room temperature. The hybrid transverse magneto-thermoelectric conversion in ATMLs is potentially available even in the absence of magnetic fields; by utilizing permanent magnets with finite remanent magnetization as a magnetic component of ATML^{37,56}, not only ANE in the ferromagnetic layers but also ONE in the thermoelectric layers can be superimposed without external magnetic fields⁵⁷, eliminating the unnecessary electricity for magnetic field applications. The interdisciplinary fusion of transverse thermoelectrics by ANE and ODSE in ATMLs will stimulate research on thermoelectric applications in the topological materials science community more actively and open new directions for thermoelectric material exploration.

Methods

Preparation of Co_2MnGa , $\text{Bi}_{0.2}\text{Sb}_{1.8}\text{Te}_3$, and Bi_2Te_3 slabs and Co_2MnGa -based ATML

To prepare Co_2MnGa ingots, 99.97% purity Co, 99.99% purity Mn, and 99.9999% purity Ga shots (RARE METALLIC Co., Ltd.) were arc-melted with an atomic ratio of 2:1:1 in an Ar atmosphere. The resulting arc-melted ingot was homogenized in high vacuum at 1000°C for 48 hours, followed by 600°C for 72 hours. Subsequently, the ingot was crushed using planetary ball mill and sieved through a 100- μm mesh. The Co_2MnGa powder was subsequently sintered into a cylindrical slab with a diameter of 20 mm at 850°C and a pressure of 30 MPa for 60 minutes in a vacuum chamber by the SPS method. $\text{Bi}_{0.2}\text{Sb}_{1.8}\text{Te}_3$ (Bi_2Te_3) ingots with a diameter of 20 mm and a height of 15 mm were prepared from 99.9% purity Bi-Sb-Te (Bi_2Te_3) powders, available from Toshima Manufacturing Co., Ltd, via the SPS method at 450°C and 30 MPa for 60 minutes under the vacuum condition. The composition ratio of sintered Bi-Sb-Te slabs was confirmed to be $\text{Bi}_{0.2}\text{Sb}_{1.8}\text{Te}_3$ using scanning electron microscopy (SEM) with energy-dispersive X-ray spectroscopy (EDS) (Cross-Beam 1540ESB, Carl Zeiss AG). The polycrystalline nature of Co_2MnGa , $\text{Bi}_{0.2}\text{Sb}_{1.8}\text{Te}_3$, and Bi_2Te_3 alloys prepared by the above procedures were also obtained by SEM-EDS. For characterization of transport properties, the Co_2MnGa ($\text{Bi}_{0.2}\text{Sb}_{1.8}\text{Te}_3$ and Bi_2Te_3) ingot was cut into a rectangular slab with a size of $\sim 10 \times 1 \times 1 \text{ mm}^3$ ($\sim 12 \times 3 \times 1 \text{ mm}^3$) using a diamond wire saw. Here, for the $\text{Bi}_{0.2}\text{Sb}_{1.8}\text{Te}_3$ and Bi_2Te_3 slabs, two rectangular slabs with different cutout directions were prepared (see Supplementary Note 2 and Fig. 8).

To fabricate Co_2MnGa -based ATMLs, the prepared cylindrical Co_2MnGa slab was sliced into many disks using the diamond wire saw. The SPS sintering for the $\text{Co}_2\text{MnGa}/\text{Bi}_{0.2}\text{Sb}_{1.8}\text{Te}_3$ and $\text{Co}_2\text{MnGa}/\text{Bi}_2\text{Te}_3$ stacks was carried out at 450°C and 30 MPa for 60 minutes in the vacuum chamber. The elemental distribution of the stacks was characterized by SEM-EDS (Supplementary Fig. 1). Finally, the prepared $\text{Co}_2\text{MnGa}/\text{Bi}_{0.2}\text{Sb}_{1.8}\text{Te}_3$ and $\text{Co}_2\text{MnGa}/\text{Bi}_2\text{Te}_3$ stacks were cut into a rectangular slab of ATML with the diamond wire saw.

Measurements of transport properties of single slab

The σ and S_S values and their H dependence of single Co_2MnGa , $\text{Bi}_{0.2}\text{Sb}_{1.8}\text{Te}_3$, and Bi_2Te_3 slabs were measured using the system similar to the Seebeck Coefficient/Electric Resistance Measurement System

(ZEM-3, ADVANCE RIKO, Inc.)^{58,59}. Here, the sample was clamped between two Cu blocks whose temperatures were independently controlled using ceramic heaters and Pt100 temperature sensors. \mathbf{H} was applied along the short axis of the samples using an electromagnet. R-type (PtRh-Pt) thermocouple probes were attached to the sample to simultaneously measure the electric voltage and temperature difference. Simultaneous measurements of the generated thermoelectric voltage and temperature difference between the two thermocouple probes in the direction parallel to the applied ∇T through the Cu blocks enables accurate estimation of S_S . The S_S value was quantified by fitting the temperature difference dependence of the thermoelectric voltage to a linear function. The magnitude of σ was evaluated via the standard four-terminal method by applying a charge current through the Cu blocks. The κ value was evaluated by multiplying the thermal diffusivity measured using the laser flash method, the specific heat using the differential scanning calorimetry, and the density using the Archimedes method. S_N was measured using a homemade temperature gradient generator combined with an electromagnet through a method similar to that described in ref. 52 (see also Supplementary Fig. 3). The sample was bridged onto two surface-anodized Al blocks, where one of the Al blocks was thermally mounted on a heat bath and the other had a chip heater to apply ∇T . The surface of the sample was coated with black ink and the magnitude of ∇T was measured with the infrared camera. While sweeping \mathbf{H} in the direction perpendicular to ∇T , generated V_T in the direction perpendicular to both ∇T and \mathbf{H} was measured. The S_N value was estimated by fitting the ∇T dependence of E_T , i.e., V_T divided by the sample width, with a linear function (Supplementary Fig. 3). All measurements were performed at room temperature and atmospheric pressure.

LIT measurements

The LIT measurements were conducted with Enhanced Lock-In Thermal Emission (ELITE, DCG Systems G.K.) at room temperature and atmospheric pressure. For the LIT measurements under the vertical \mathbf{H} , the ATML samples were directly mounted on the center of an electromagnet to ensure the uniform H . For the LIT measurements under the horizontal \mathbf{H} , the ATML samples were securely mounted on a phenolic resin plate with low thermal conductivity to minimize the heat leakage through thermal conduction. To improve infrared emissivity and ensure uniform emission properties during the LIT measurements, the top and side surfaces of the samples were coated with insulating black ink whose emissivity is >0.94 (JSC-3, JAPANSENSOR Corporation). The minimum f value during the LIT measurements was determined by considering the thermal boundary conditions; we chose 0.2 Hz as a minimum f because we have confirmed that there is no influence of parasitic signals, such as the Peltier effect at the sample edges due to wiring, to the signal on the sample in the viewing area of LIT at 0.2 Hz. The viewing area of all the lock-in images is 512×260 pixels = 7.68×3.90 mm².

Measurements of transverse thermopower in Co₂MnGa-based ATMLs

A schematic of the measurement set-up for the transverse thermopower in Co₂MnGa-based ATMLs is shown in the inset of Fig. 7c. The ATML samples for thermopower measurements were fixed on a heat bath made of a surface-anodized Al block. To apply ∇T to the samples, a chip heater was attached to the top surface of

the sample and a sapphire substrate was inserted between the heater and sample to ensure uniform temperature gradient application. The ∇T value was determined using the infrared camera by coating the side surface of the sample with the black ink. During sweeping \mathbf{H} in the width direction of the samples perpendicular to ∇T , V_T in the longitudinal direction was measured. Finally, the S_T value was quantified by linear fitting of E_T - ∇T plots, where $E_T = V_T/l\nabla T$ with l representing the longitudinal length of the sample.

Data availability

The data that support the findings of this study are available from the corresponding authors upon reasonable request.

References

1. Bell, L. E. Cooling, heating, generating power, and recovering waste heat with thermoelectric systems. *Science* **321**, 1457–1461 (2008).
2. Snyder, G. J. & Toberer, E. S. Complex TE materials. *Nat. Mater.* **7**, 105–114 (2008).
3. Yang, L., Chen, Z., Dargusch, M. S. & Zou, J. High performance thermoelectric materials: Progress and their applications. *Adv. Energy Mater.* **8**, 1701797 (2018).
4. Uchida, K. & Heremans, J. P. Thermoelectrics: from longitudinal to transverse. *Joule* **6**, 2240 (2022).
5. Sakuraba, Y. Potential of thermoelectric power generation using anomalous Nernst effect in magnetic materials. *Scr. Mater.* **111**, 29 (2016).
6. Uchida, K., Zhou, W. & Sakuraba, Y. Transverse thermoelectric generation using magnetic materials. *Appl. Phys. Lett.* **118**, 140504 (2021).
7. Miyasato, T. et al. Crossover behavior of the anomalous Hall effect and anomalous Nernst effect in itinerant ferromagnets. *Phys. Rev. Lett.* **99**, 086602 (2007).
8. Ramos, R. et al. Anomalous Nernst effect of Fe_3O_4 single crystal. *Phys. Rev. B* **90**, 054422 (2014).
9. Hasegawa, K. et al. Material dependence of anomalous Nernst effect in perpendicularly magnetized ordered-alloy thin films. *Appl. Phys. Lett.* **106**, 252405 (2015).
10. Xu, J., Phelan, W. A. & Chien, C. L. Large Anomalous Nernst effect in a van der Waals ferromagnet Fe_3GeTe_2 . *Nano Lett.* **19**, 8250–8254 (2019).
11. Miura, A. et al. Observation of anomalous Ettingshausen effect and large transverse thermoelectric conductivity in permanent magnets. *Appl. Phys. Lett.* **115**, 222403 (2019).
12. Miura, A. et al. High-temperature dependence of anomalous Ettingshausen effect in SmCo_5 -type permanent magnets. *Appl. Phys. Lett.* **117**, 082408 (2020).
13. Ando, F., Hirai, T. & Uchida, K. Permanent-magnet-based transverse thermoelectric generator with high fill factor driven by anomalous Nernst effect. *APL Energy* **2**, 016103 (2024).
14. Gautam, R. et al. Creation of flexible spin-caloritronic material with giant transverse thermoelectric conversion by nanostructure engineering. *Nat. Commun.* **15**, 2184 (2024).
15. Behnia, K. & Aubin, H. Nernst effect in metals and superconductors: A review of concepts and experiments. *Reports Prog. Phys.* **79**, 046502 (2016).

16. Ikhlas, M. et al. Large anomalous Nernst effect at room temperature in a chiral antiferromagnet. *Nat. Phys.* **13**, 1085–1090 (2017).
17. Liang, T. et al. Anomalous Nernst effect in the Dirac semimetal Cd₃As₂. *Phys. Rev. Lett.* **118**, 136601 (2017).
18. Reichlova, H. et al. Large anomalous Nernst effect in thin films of the Weyl semimetal Co₂MnGa. *Appl. Phys. Lett.* **113**, 212405 (2018).
19. Sakai, A. et al. Giant anomalous Nernst effect and quantum-critical scaling in a ferromagnetic semimetal. *Nat. Phys.* **14**, 1119–1124 (2018).
20. Ding, L. et al. Intrinsic anomalous Nernst effect amplified by disorder in a half-metallic semimetal. *Phys. Rev. X* **9**, 041061 (2019).
21. Nakayama, H. et al. Mechanism of strong enhancement of anomalous Nernst effect in Fe by Ga substitution. *Phys. Rev. Mater.* **3**, 114412 (2019).
22. Asaba, T. et al. Colossal anomalous Nernst effect in a correlated noncentrosymmetric kagome ferromagnet. *Sci. Adv.* **7**, eabf1467 (2021).
23. Pan, Y. et al. Giant anomalous Nernst signal in the antiferromagnet YbMnBi₂. *Nat. Mater.* **21**, 203–209 (2022).
24. Chen, T. et al. Large anomalous Nernst effect and nodal plane in an iron-based kagome ferromagnet. *Sci. Adv.* **8**, eabk1480 (2022).
25. Noguchi, S. et al. Bipolarity of large anomalous Nernst effect in Weyl magnet-based alloy films. *Nat. Phys.* **20**, 254–260 (2024).
26. Xu, L. et al. Anomalous transverse response of Co₂MnGa and universality of the room-temperature $\alpha_{ij}^A/\sigma_{ij}^A$ ratio across topological magnets. *Phys. Rev. B* **101**, 180404(R) (2020).
27. Zahner, T., Förg, R. & Lengfellner, H. Transverse thermoelectric response of a tilted metallic multilayer structure. *Appl. Phys. Lett.* **73**, 1364–1366 (1998).
28. Kyarad, A. & Lengfellner, H. Transverse Peltier effect in tilted Pb-Bi₂Te₃ multilayer structures. *Appl. Phys. Lett.* **89**, 192103 (2006).
29. Kanno, T., Yotsuhashi, S., Sakai, A., Takahashi, K. & Adachi, H. Enhancement of transverse thermoelectric power factor in tilted Bi/Cu multilayer. *Appl. Phys. Lett.* **94**, 061917 (2009).
30. Goldsmid, H. J. Application of the transverse thermoelectric effects. *J. Electron. Mater.* **40**, 1254–1259 (2011).
31. Sakai, A. et al. Breaking the trade-off between thermal and electrical conductivities in the thermoelectric material of an artificially tilted multilayer. *Sci. Rep.* **4**, 6089 (2014).
32. Mu, X. et al. High-performance YbAl₃/Bi_{0.5}Sb_{1.5}Te₃ artificially tilted multilayer thermoelectric devices via material genome engineering method. *J. Power Sources* **430**, 193–200 (2019).
33. Li, Y. et al. Geometrical structure optimization design of high-performance Bi₂Te₃-based artificially tilted multilayer thermoelectric devices. *J. Electron. Mater.* **49**, 5980–5988 (2020).
34. Zhu, W. et al. Fabrication and performance prediction of Ni/Bi_{0.5}Sb_{1.5}Te₃ artificially-tilted multilayer devices with transverse thermoelectric effect. *J. Power Sources* **512**, 230471 (2021).
35. Yue, K. et al. High transverse thermoelectric performance and interfacial stability of Co/Bi_{0.5}Sb_{1.5}Te₃ artificially tilted multilayer thermoelectric devices. *ACS Appl. Mater. Interfaces* **14**, 39053–39061 (2022).
36. Zhou, H. et al. Geometrical optimization and transverse thermoelectric performances of Fe/Bi₂Te_{2.7}Se_{0.3} artificially tilted multilayer thermoelectric devices. *Micromachines* **13**, 233 (2022).

37. Uchida, K., Hirai, T., Ando, F. & Sepehri-Amin, H. Hybrid transverse magneto-thermoelectric cooling in artificially tilted multilayers. *Adv. Energy Mater.* **14**, 2302375 (2024).
38. Guin, S. N. et al. Anomalous Nernst effect beyond the magnetization scaling relation in the ferromagnetic Heusler compound Co_2MnGa . *NPG Asia Mater.* **11**, 16 (2019).
39. Sumida, K. et al. Spin-polarized Weyl cones and giant anomalous Nernst effect in ferromagnetic Heusler films. *Commun. Mater.* **1**, 89 (2020).
40. Zhou, W., Miura, A., Hirai, T., Sakuraba, Y. & Uchida, K. Seebeck-driven transverse thermoelectric generation in magnetic hybrid bulk materials. *Appl. Phys. Lett.* **122**, 062402 (2023).
41. Wei, J. et al. Review of current high-ZT thermoelectric materials. *J. Mater. Sci.* **55**, 12642–12704 (2020).
42. Chen, M. et al. Topological Heusler magnets-driven high-performance transverse Nernst thermoelectric generators. *Adv. Energy Mater.* 2400411 (2024).
43. Breitenstein, O., Warta, W. & Langenkamp, M. *Lock-in Thermography: Basics and Use for Evaluating Electronic Devices and Materials*. (Springer, Berlin, Heidelberg, 2010).
44. Daimon, S., Iguchi, R., Hioki, T., Saitoh, E. & Uchida, K. Thermal imaging of spin Peltier effect. *Nat. Commun.* **7**, 13754 (2016).
45. Seki, T., Iguchi, R., Takanashi, K. & Uchida, K. Visualization of anomalous Ettingshausen effect in a ferromagnetic film: Direct evidence of different symmetry from spin Peltier effect. *Appl. Phys. Lett.* **112**, 152403 (2018).
46. Uchida, K., Daimon, S., Iguchi, R. & Saitoh, E. Observation of anisotropic magneto-Peltier effect in nickel. *Nature* **558**, 95–99 (2018).
47. Hirai, T. et al. Strain-induced cooling-heating switching of anisotropic magneto-Peltier effect. *Appl. Phys. Lett.* **118**, 022403 (2021).
48. Hirai, T., Iguchi, R., Miura, A. & Uchida, K. Elastocaloric kirigami temperature modulator. *Adv. Funct. Mater.* **32**, 2201116 (2022).
49. Straube, H., Wagner, J. M. & Breitenstein, O. Measurement of the Peltier coefficient of semiconductors by lock-in thermography. *Appl. Phys. Lett.* **95**, 052107 (2009).
50. Alasli, A., Miura, A., Iguchi, R., Nagano, H. & Uchida, K. High-throughput imaging measurements of thermoelectric figure of merit. *Sci. Technol. Adv. Mater. Methods* **1**, 162–168 (2021).
51. Uchida, K., Murata, M., Miura, A. & Iguchi, R. Observation of the magneto-Thomson effect. *Phys. Rev. Lett.* **125**, 106601 (2020).
52. Zhou, W. et al. Seebeck-driven transverse thermoelectric generation. *Nat. Mater.* **20**, 463–467 (2021).
53. Zhou, W., Sasaki, T., Uchida, K. & Sakuraba, Y. Direct-contact Seebeck-driven transverse magneto-thermoelectric generation in magnetic/thermoelectric bilayers. *Adv. Sci.* 2308543 (2024).
54. Yamamoto, K. et al. Phenomenological analysis of transverse thermoelectric generation and cooling performance in magnetic/thermoelectric hybrid systems. *J. Appl. Phys.* **129**, 223908 (2021).
55. Uchida, K. et al. Enhancement of anomalous Nernst effects in metallic multilayers free from proximity-induced magnetism. *Phys. Rev. B* **92**, 094414 (2015).
56. Ando, F. et al. Multifunctional composite magnet for practical transverse thermoelectrics. Preprint at <https://arxiv.org/abs/2402.18019> (2024).

57. Murata, M., Hirai, T., Seki, T. & Uchida, K. Zero-magnetic-field operation of ordinary-Nernst-effect-based transverse thermoelectric module using embedded permanent magnets. *Appl. Phys. Lett.* **124**, 193901 (2024).
58. Hirai, T. et al. Temperature dependence of anisotropic magneto-Seebeck effect in NiPt alloys. *Appl. Phys. Express* **14**, 073001 (2021).
59. Hirai, T., Sakuraba, Y. & Uchida, K. Observation of the giant magneto-Seebeck effect in a metastable $\text{Co}_{50}\text{Fe}_{50}/\text{Cu}$ multilayer. *Appl. Phys. Lett.* **121**, 162404 (2022).

Acknowledgements

The authors thank T. Seki, Y. Sakuraba, W. Zhou, F. Makino, K. Suzuki, and M. Isomura for technical support and valuable discussions. This work was partially supported by ERATO “Magnetic Thermal Management Materials Project” (No. JPMJER2201) from JST, Japan; Grant-in-Aid for Scientific Research (S) (No. 22H04965) from JSPS KAKENHI, Japan; and NEC Corporation.

Author contributions

T.H. and K.U. planned and designed the experiments, prepared the samples, and performed the LIT experiments. T.H. analyzed the LIT data, measured the thermoelectric, electric, thermal transport properties of the samples, and developed the explanation of the experimental results. K.U. collected magnetic properties of ATMLs. F.A. analytically simulated the transport properties in ATMLs. H.S.A conducted the microstructural characterization. T.H. and K.U. wrote the manuscript. K.U. supervised the project. All authors discussed the results and commented on the manuscript.

Competing interests

The authors declare no competing interests.

Additional information

Correspondence and requests for materials should be addressed to Takamasa Hirai or Ken-ichi Uchida.

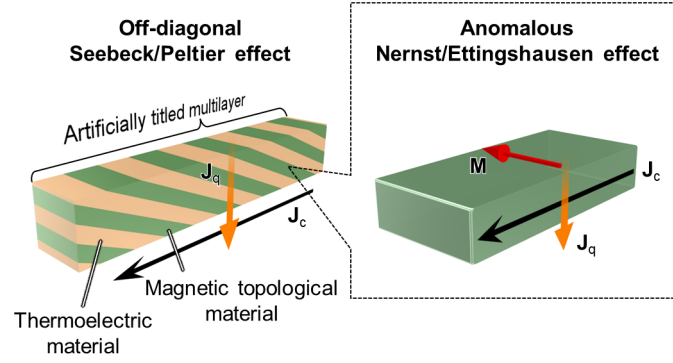


Fig. 1 | Hybrid transverse magneto-thermoelectric conversion in artificially tilted multilayers using magnetic topological materials. Schematics of the off-diagonal Seebeck/Peltier effect (ODSE/ODPE) in an artificially tilted multilayer (ATML) comprising magnetic and thermoelectric materials and the anomalous Nernst/Ettingshausen effect (ANE/AEE) in the magnetic material. Here, \mathbf{J}_c , \mathbf{J}_q , and \mathbf{M} denote the charge current, heat current, and magnetization, respectively.

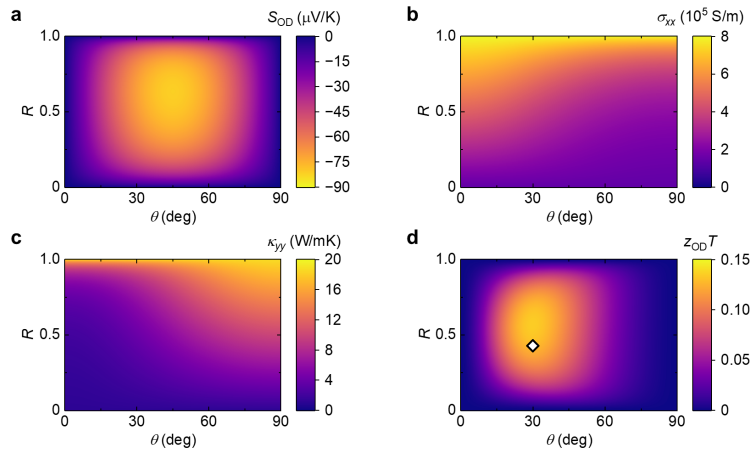
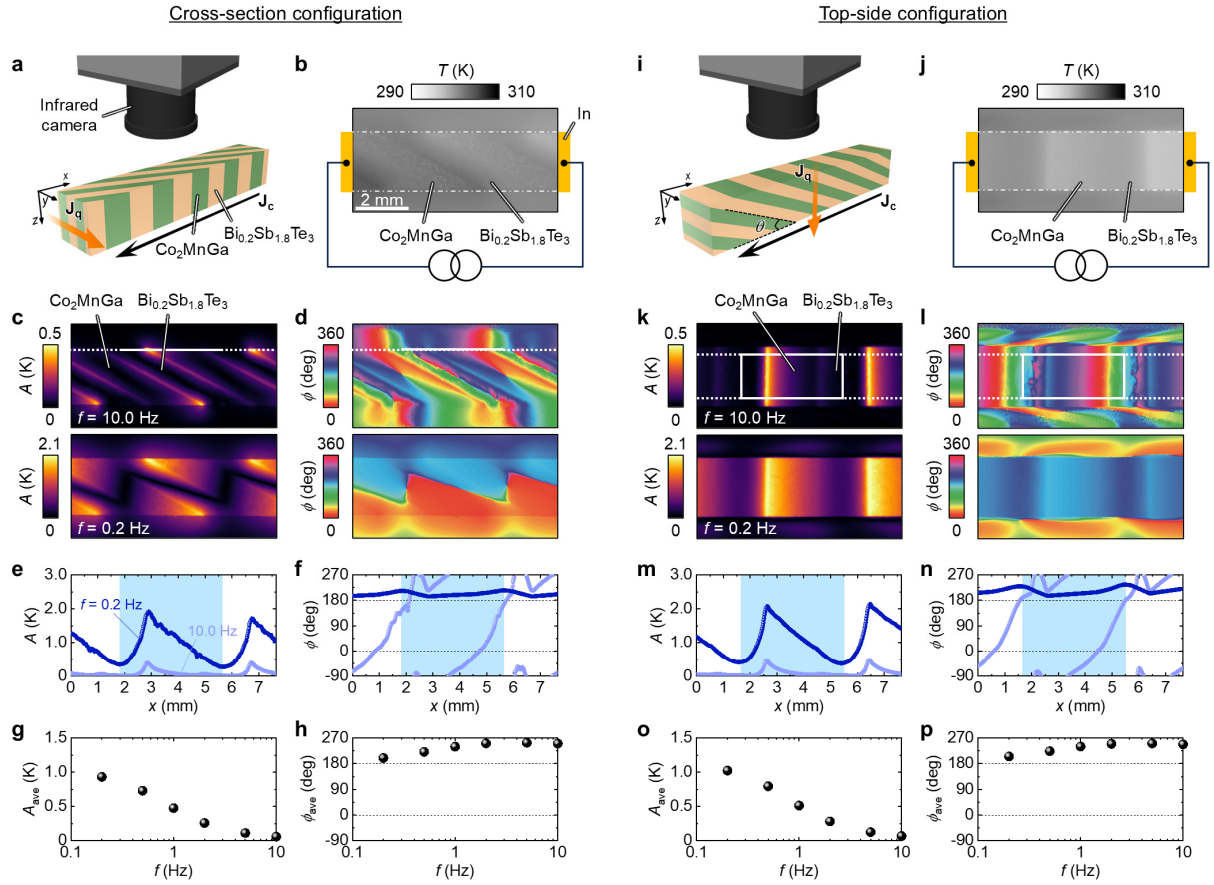


Fig. 2 | Simulation of transverse thermopower and electrical/thermal conductivity for $\text{Co}_2\text{MnGa}/\text{Bi}_{0.2}\text{Sb}_{1.8}\text{Te}_3$ ATML. **a-d** Contour maps depicting the transverse thermopower due to ODSE S_{OD} (**a**), electrical conductivity along the \mathbf{J}_c direction σ_{xx} (**b**), thermal conductivity along the \mathbf{J}_q direction κ_{yy} (**c**), and dimensionless figure of merit for ODSE $z_{\text{OD}}T (= S_{\text{OD}}^2 \sigma_{xx} T / \kappa_{yy})$ at zero magnetic field and the temperature $T = 300$ K (**d**) as functions of the tilt angle of ATML θ and thickness ratio R defined as $R = t_M / (t_M + t_{\text{TE}})$ with $t_{\text{M(TE)}}$ being the thickness of the magnetic (thermoelectric) layer. The open diamond symbol in (**d**) represents the $\theta (= 30^\circ \pm 1^\circ)$ and $R (= 0.43)$ values for our sample. θ was estimated from the thermal images obtained for lock-in thermography (LIT).



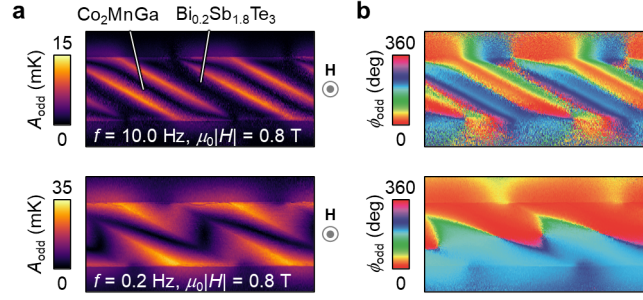


Fig. 4 | Contribution of transverse magneto-thermoelectric effects in $\text{Co}_2\text{MnGa}/\text{Bi}_{0.2}\text{Sb}_{1.8}\text{Te}_3$ ATML in cross-section configuration. a,b H -odd-dependent component of the lock-in amplitude A_{odd} (a) and phase ϕ_{odd} (b) images at $\mu_0|H| = 0.8$ T and $f = 10.0$ and 0.2 Hz in $\text{Co}_2\text{MnGa}/\text{Bi}_{0.2}\text{Sb}_{1.8}\text{Te}_3$ ATML. Here, the magnetic field \mathbf{H} with the magnitude of H was applied along the vertical direction (z axis in Fig. 3a) of the sample and μ_0 is the vacuum permeability.

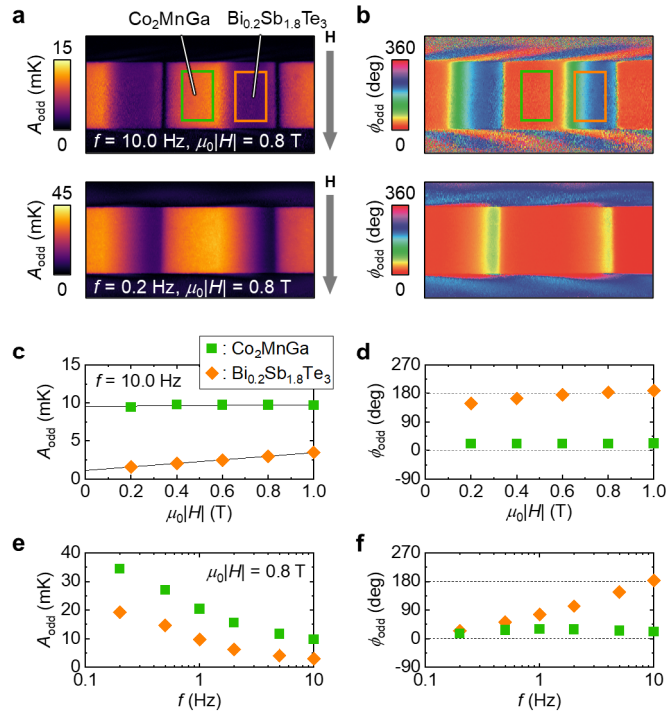


Fig. 5 | Contribution of transverse magneto-thermoelectric effects in $\text{Co}_2\text{MnGa}/\text{Bi}_{0.2}\text{Sb}_{1.8}\text{Te}_3$ ATML in top-side configuration. a,b A_{odd} (a) and ϕ_{odd} (b) images at $\mu_0|H| = 0.8$ T and $f = 10.0$ and 0.2 Hz in $\text{Co}_2\text{MnGa}/\text{Bi}_{0.2}\text{Sb}_{1.8}\text{Te}_3$ ATML. Here, \mathbf{H} was applied along the horizontal short direction of the sample (y axis in Fig. 3i). **c,d** $|H|$ dependence of A_{odd} (c) and ϕ_{odd} (d) at $f = 10.0$ Hz. Solid lines in c represent the results of linear fitting. **e,f** f dependence of A_{odd} (e) and ϕ_{odd} (f) at $\mu_0|H| = 0.8$ T. The data points in c-f were obtained by averaging the temperature modulation signal in the area defined by the green and orange rectangles in a and b for the Co_2MnGa and $\text{Bi}_{0.2}\text{Sb}_{1.8}\text{Te}_3$ areas, respectively.

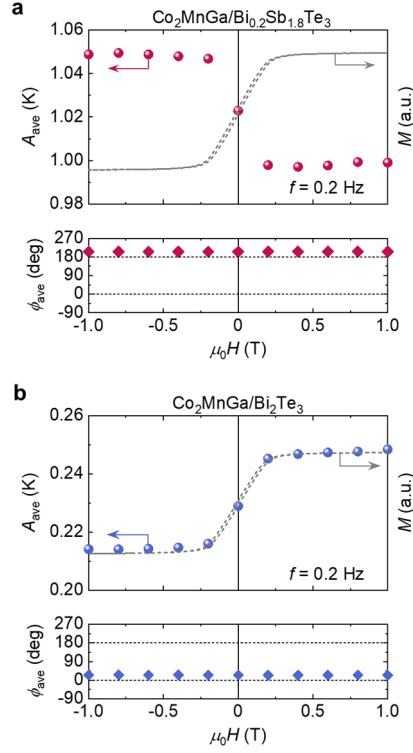


Fig. 6 | Hybrid transverse magneto-thermoelectric temperature modulation in Co₂MnGa-based ATML. H dependence of the averaged A_{ave} and ϕ_{ave} signals at $f = 0.2$ Hz for Co₂MnGa/Bi_{0.2}Sb_{1.8}Te₃ (a) and Co₂MnGa/Bi₂Te₃ (b) ATMLs. The magnetization M curves of Co₂MnGa in each ATML measured using a vibrating sample magnetometer are also shown (note that Bi_{0.2}Sb_{1.8}Te₃ and Bi₂Te₃ are nonmagnetic).

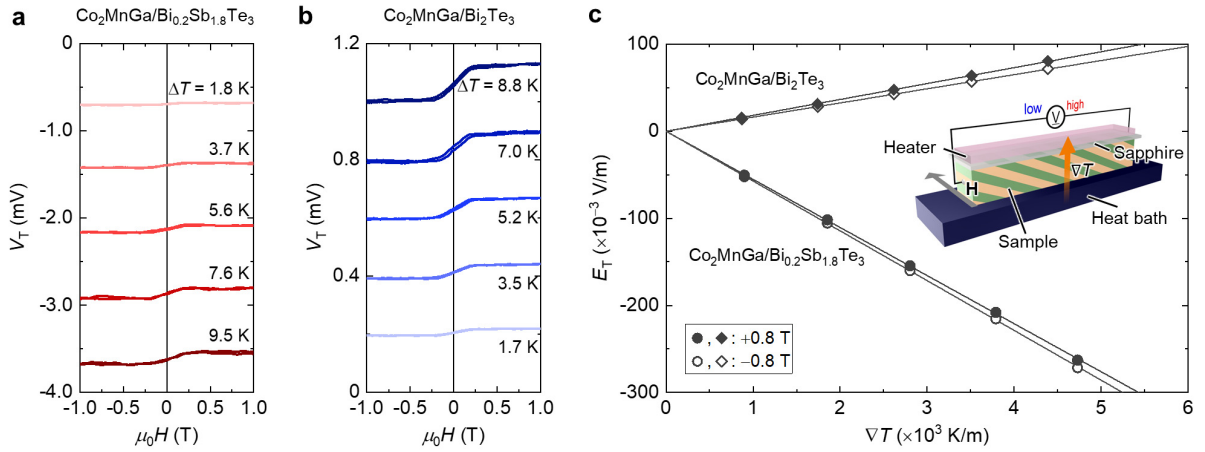


Fig. 7 | Hybrid transverse magneto-thermoelectric generation in Co₂MnGa-based ATML. a,b H dependence of the transverse thermoelectric voltage V_T at various ΔT values for Co₂MnGa/Bi_{0.2}Sb_{1.8}Te₃ (a) and Co₂MnGa/Bi₂Te₃ (b) ATMLs. ΔT denotes the temperature difference between the top and bottom surfaces of ATML. c ∇T dependence of the transverse electric field E_T ($= V_T/l$) for Co₂MnGa/Bi_{0.2}Sb_{1.8}Te₃ and Co₂MnGa/Bi₂Te₃ ATMLs at $\mu_0 H = \pm 0.8$ T. ∇T and l denote temperature gradient and sample length, respectively. The transverse thermopower S_T , estimated by linear fitting, is -55.2 ($+18.3$) $\mu\text{V/K}$ at $+0.8$ T and -57.1 ($+16.2$) $\mu\text{V/K}$ at -0.8 T for Co₂MnGa/Bi_{0.2}Sb_{1.8}Te₃ (Co₂MnGa/Bi₂Te₃) ATML. The inset shows a schematic of the set-up for measuring the transverse thermopower.

Supplementary Information for “Hybridizing anomalous Nernst effect in artificially tilted multilayer based on magnetic topological material”

Table of contents

Supplementary Note 1 | Calculation of transport properties in artificially tilted multilayers.

Supplementary Note 2 | Anisotropy of electric and thermoelectric transport properties in sintered $\text{Bi}_{0.2}\text{Sb}_{1.8}\text{Te}_3$ and Bi_2Te_3 .

Supplementary Table 1 | Transport properties of Co_2MnGa , $\text{Bi}_{0.2}\text{Sb}_{1.8}\text{Te}_3$, and Bi_2Te_3 slabs.

Supplementary Fig. 1 | Structural and chemical characterization in Co_2MnGa -based multilayers.

Supplementary Fig. 2 | Measurements of the Nernst effect.

Supplementary Fig. 3 | Simulation of transverse thermopower and electrical/thermal conductivity for $\text{Co}_2\text{MnGa}/\text{Bi}_2\text{Te}_3$ ATML.

Supplementary Fig. 4 | Transverse thermoelectric conversion in $\text{Co}_2\text{MnGa}/\text{Bi}_2\text{Te}_3$ ATML at zero magnetic field.

Supplementary Fig. 5 | Contribution of transverse magneto-thermoelectric effects in $\text{Co}_2\text{MnGa}/\text{Bi}_2\text{Te}_3$ ATML in cross-section configuration.

Supplementary Fig. 6 | Contribution of transverse magneto-thermoelectric effects in $\text{Co}_2\text{MnGa}/\text{Bi}_2\text{Te}_3$ ATML in top-side configuration.

Supplementary Fig. 7 | Simulation of dimensionless figure of merit for transverse thermoelectric generation with hybridized ODSE and ANE in ATML.

Supplementary Fig. 8 | Dependence of electrical and thermoelectric transport properties of sintered $\text{Bi}_{0.2}\text{Sb}_{1.8}\text{Te}_3$ and Bi_2Te_3 on pressing direction.

Supplementary References

Note 1 | Calculation of transport properties in artificially tilted multilayers.

Referring to ref. 1 and 2 in Supplementary Information, the thermoelectric, electrical, thermal transport parameters of magnetic/thermoelectric multilayers in the direction parallel (S_{\parallel} , σ_{\parallel} , and κ_{\parallel}) and perpendicular (S_{\perp} , σ_{\perp} , and κ_{\perp}) to the stacking plane are formulated using the following Supplementary Equations (1)-(3) on the assumption that the interfacial electrical and thermal resistances at boundaries between magnetic and thermoelectric layers are negligibly small:

$$S_{\parallel} = \frac{R\sigma_M S_{S,M} + (1-R)\sigma_{TE} S_{S,TE}}{R\sigma_M + (1-R)\sigma_{TE}}, \quad S_{\perp} = \frac{R\kappa_{TE} S_{S,M} + (1-R)\kappa_M S_{S,TE}}{R\kappa_{TE} + (1-R)\kappa_M} \quad (1)$$

$$\sigma_{\parallel} = R\sigma_M + (1-R)\sigma_{TE}, \quad \sigma_{\perp} = \frac{\sigma_M \sigma_{TE}}{(1-R)\sigma_M + R\sigma_{TE}} \quad (2)$$

$$\kappa_{\parallel} = R\kappa_M + (1-R)\kappa_{TE}, \quad \kappa_{\perp} = \frac{\kappa_M \kappa_{TE}}{(1-R)\kappa_M + R\kappa_{TE}} \quad (3)$$

Here, $S_{S,M}$ ($S_{S,TE}$) is the Seebeck coefficient, σ_M (σ_{TE}) the electrical conductivity, and κ_M (κ_{TE}) the thermal conductivity of the magnetic (thermoelectric) component and $R [= t_M/(t_M+t_{TE})]$ is the thickness ratio with t_M (t_{TE}) being the thickness of the magnetic (thermoelectric) component. When the magnetic/thermoelectric stacks are rotated with the tilt angle θ to form artificially tilted multilayers (ATMLs), the transverse thermopower due to the off-diagonal Seebeck effect (ODSE), S_{OD} , and the electrical and thermal conductivities orthogonal to each other (σ_{xx} and κ_{yy}) are respectively expressed as

$$S_{OD} = (S_{\perp} - S_{\parallel}) \sin \theta \cos \theta \quad (4)$$

$$\sigma_{xx} = \frac{\sigma_{\parallel} \sigma_{\perp}}{\sigma_{\parallel} \sin^2 \theta + \sigma_{\perp} \cos^2 \theta} \quad (5)$$

$$\kappa_{yy} = \kappa_{\parallel} \sin^2 \theta + \kappa_{\perp} \cos^2 \theta \quad (6)$$

With these parameters, the dimensionless figure of merit for ODSE $z_{OD}T$ with T being the absolute temperature is defined as

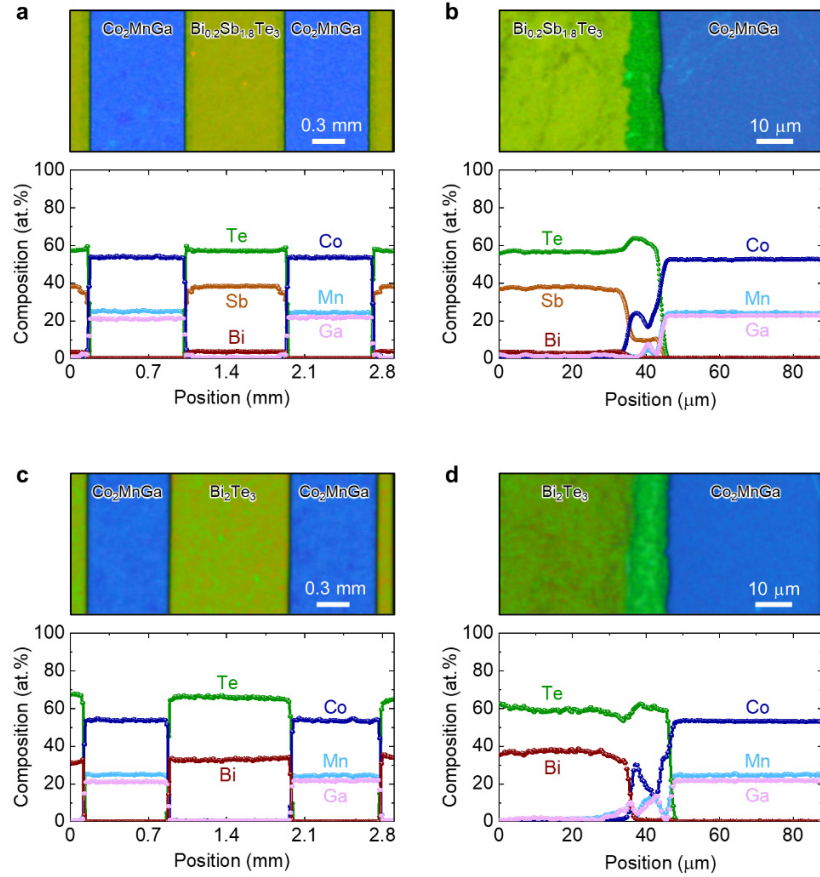
$$z_{OD}T = \frac{S_{OD}^2 \sigma_{xx}}{\kappa_{yy}} T \quad (7)$$

Note 2 | Anisotropy of electric and thermoelectric transport properties in sintered $\text{Bi}_{0.2}\text{Sb}_{1.8}\text{Te}_3$ and Bi_2Te_3 .

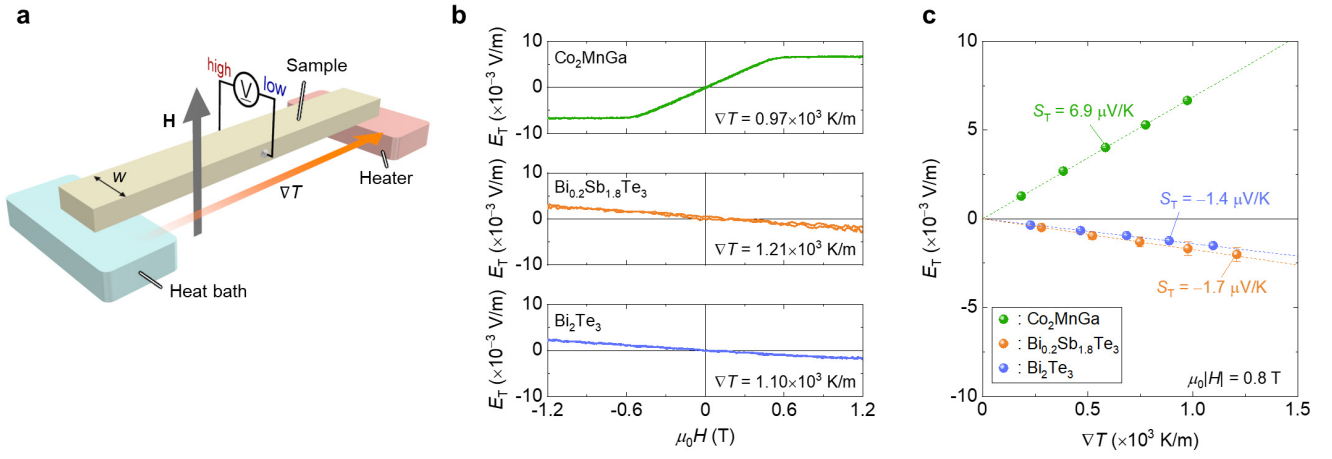
From the sintered cylindrical Bi_2Te_3 and $\text{Bi}_{0.2}\text{Sb}_{1.8}\text{Te}_3$ ingots with a diameter of 20 mm and a height of 15 mm, two rectangular slabs, named ‘‘Slab 1’’ and ‘‘Slab 2’’, with a size of $\sim 12 \times 3 \times 1 \text{ mm}^3$ were cut out using the diamond wire saw, where the longitudinal direction of Slab1 (Slab2) was along the diameter (height) direction of the ingot, i.e., perpendicular (parallel) to the pressing direction during spark plasma sintering (SPS) (Supplementary Fig. 7a). Supplementary Fig. 7b shows the Seebeck coefficient S_S and electrical conductivity σ of Slabs 1 and 2 for Bi_2Te_3 and $\text{Bi}_{0.2}\text{Sb}_{1.8}\text{Te}_3$. In both the Bi_2Te_3 and $\text{Bi}_{0.2}\text{Sb}_{1.8}\text{Te}_3$ slabs, there was little difference in S_S between Slabs 1 and 2, while the magnitude of σ of Slab 2 was clearly smaller than that of Slab 1 even though our $\text{Bi}_{0.2}\text{Sb}_{1.8}\text{Te}_3$ and Bi_2Te_3 slabs are polycrystalline. The behavior of isotropic S_S and anisotropic σ in Bi-Sb-Te and Bi-Te prepared by SPS has been also reported in the previous study; it is not due to their intrinsic band structure but due to the particle shape of the matrix powder³. However, the observed anisotropy of σ has little impact on the transport properties of our ATMLs; the value of dimensionless figure of merit for the off-diagonal Seebeck effect calculated with the parameters for Slab 1 was almost the same as that for Slab 2 (Supplementary Fig. 7c,d and Supplementary Note 1 for calculation details).

Table 1 | Transport properties of Co_2MnGa , $\text{Bi}_{0.2}\text{Sb}_{1.8}\text{Te}_3$, and Bi_2Te_3 slabs. The value of σ , thermal conductivity κ , thermal diffusivity D , specific heat C , density ρ , S_S , ordinary or anomalous Nernst coefficient S_N at the magnetic field $\mu_0|H| = 0$ and 0.8 T with μ_0 and H being the vacuum permeability and magnitude of the magnetic field, respectively.

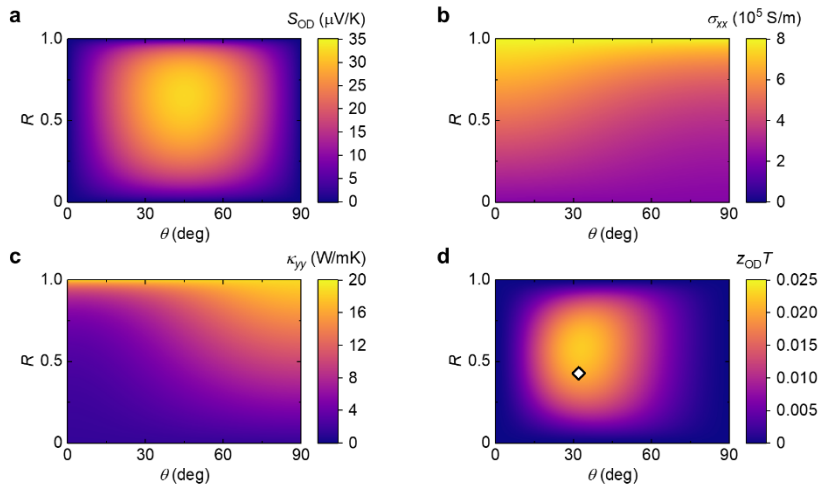
	Co_2MnGa		$\text{Bi}_{0.2}\text{Sb}_{1.8}\text{Te}_3$		Bi_2Te_3	
	$\mu_0 H = 0$ T	0.8 T	0 T	0.8 T	0 T	0.8 T
$\sigma (\times 10^5 \text{ S/m})$	7.99	8.00	1.28	1.28	1.83	1.83
$\kappa (\text{W/mK})$	18.7	n/a	1.2	n/a	1.5	n/a
$D (\times 10^{-6} \text{ m}^2/\text{s})$	5.17	n/a	0.86	n/a	1.14	n/a
$C (\text{J/gK})$	0.44	n/a	0.22	n/a	0.18	n/a
$\rho (\times 10^6 \text{ g/m}^3)$	8.33	n/a	6.37	n/a	7.12	n/a
$S_S (\mu\text{V/K})$	-32.1 ± 0.5	-32.0 ± 0.5	170.6 ± 0.5	170.5 ± 0.5	-110.3 ± 0.7	-109.7 ± 0.6
$S_N (\mu\text{V/K})$	n/a	6.9 ± 0.2	n/a	-1.7 ± 0.3	n/a	-1.4 ± 0.1



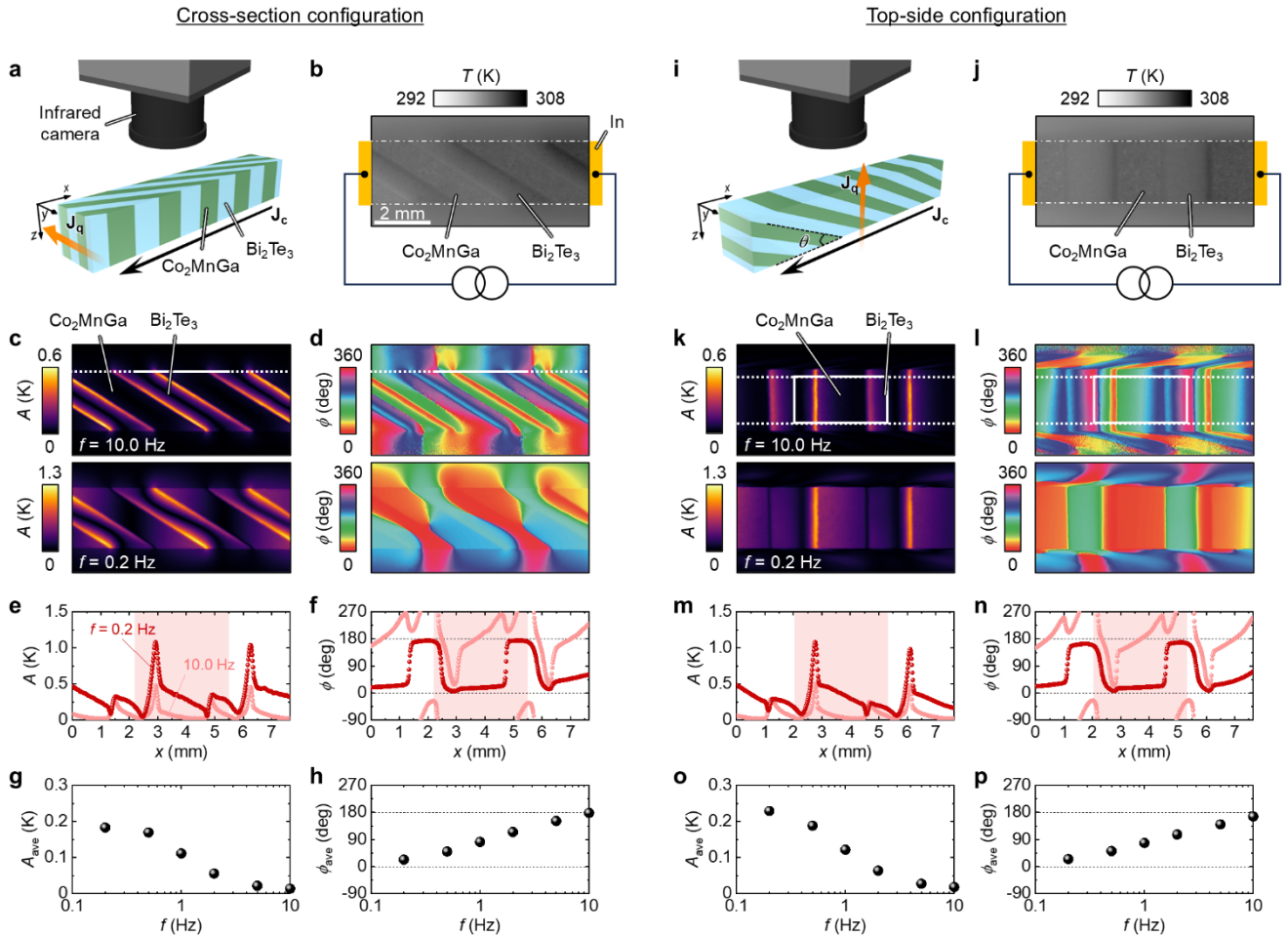
Supplementary Fig. 1 | Structural and chemical characterization in Co_2MnGa -based multilayers. **a,b** Cross-sectional scanning electron microscopy with energy-dispersive X-ray spectroscopy mapping images for the $\text{Co}_2\text{MnGa}/\text{Bi}_{0.2}\text{Sb}_{1.8}\text{Te}_3$ multilayer with low **(a)** and high **(b)** magnification. Line profiles of the atomic composition across the stacking direction in the mapping images are also shown. **c,d** Results for the $\text{Co}_2\text{MnGa}/\text{Bi}_2\text{Te}_3$ multilayer.



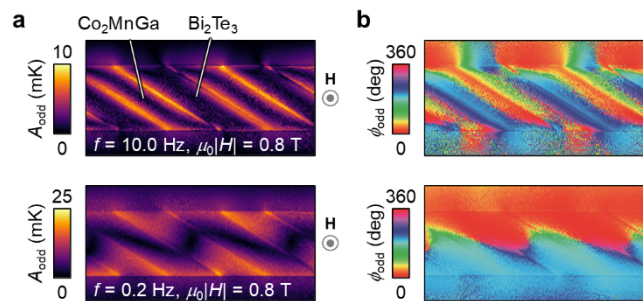
Supplementary Fig. 2 | Measurements of the Nernst effect. **a** Schematic of the set-up for measuring transverse thermoelectric voltage V_T due to the ordinary or anomalous Nernst effect, where \mathbf{H} , ∇T , and w denote the magnetic field vector, temperature gradient, and sample width, respectively. **b** H dependence of the transverse electric field E_T ($= V_T/w$) for the Co_2MnGa , $\text{Bi}_{0.2}\text{Sb}_{1.8}\text{Te}_3$, and Bi_2Te_3 slabs at $\nabla T = 0.97 \times 10^3$, 1.21×10^3 , and 1.10×10^3 K/m, respectively. The value of ∇T was measured by the infrared camera (see Methods). **c** ∇T dependence of E_T for the Co_2MnGa , $\text{Bi}_{0.2}\text{Sb}_{1.8}\text{Te}_3$, and Bi_2Te_3 slabs at $\mu_0 |H| = 0.8$ T. Dotted lines show the results of linear fitting to determine S_N .



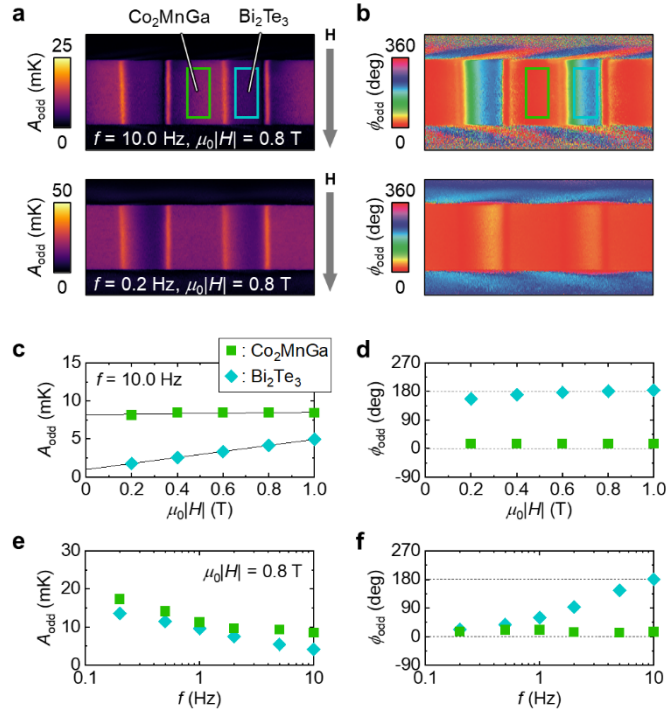
Supplementary Fig. 3 | Simulation of transverse thermopower and electrical/thermal conductivity for $\text{Co}_2\text{MnGa}/\text{Bi}_2\text{Te}_3$ ATML. **a-d** Contour maps depicting S_{OD} (**a**), σ_{xx} (**b**), κ_{yy} (**c**), and $z_{\text{OD}} T$ at zero magnetic field and $T = 300$ K (**d**) as functions of θ and R . The open diamond symbol in (**d**) represents the $\theta (= 32^\circ \pm 1^\circ)$ and $R (= 0.43)$ values.



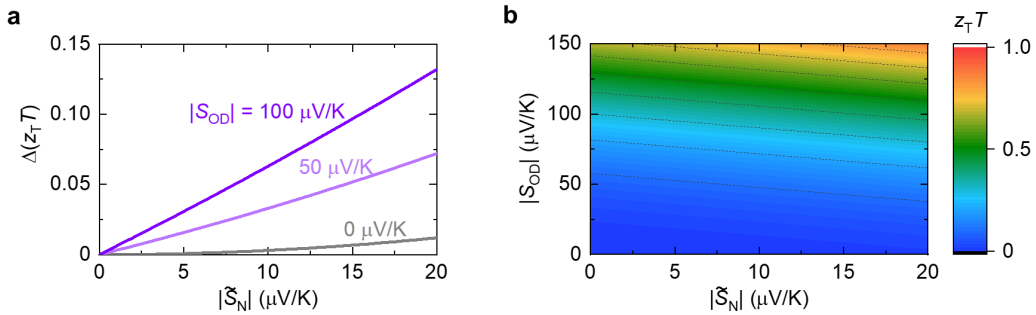
Supplementary Fig. 4 | Transverse thermoelectric conversion in $\text{Co}_2\text{MnGa}/\text{Bi}_2\text{Te}_3$ ATML at zero magnetic field. **a** Schematic of the sample structure in the cross-section configuration. **b** Steady-state temperature image during the LIT measurement in the cross-section configuration. **c,d** Lock-in amplitude A (**c**) and phase ϕ (**d**) images at the lock-in frequency $f = 10.0$ and 0.2 Hz. **e,f** x -directional A (**e**) and ϕ (**f**) profiles along the white dotted lines in the top panels of **c** and **d**, respectively. **g,h** f dependence of the averaged lock-in amplitude A_{ave} (**g**) and phase ϕ_{ave} (**h**) values over one $\text{Co}_2\text{MnGa}/\text{Bi}_2\text{Te}_3$ unit. **i-p** Results for the top-side configuration. The A_{ave} and ϕ_{ave} values in **g** and **h** (**o** and **p**) were estimated by averaging A and ϕ signals in the areas defined by the white rectangles in **c** and **d** (**k** and **l**), corresponding to the blue shaded area in **e** and **f** (**m** and **n**), respectively. In all the LIT measurements, a square-wave-modulated charge current with an amplitude of 1 A and zero offset was applied.



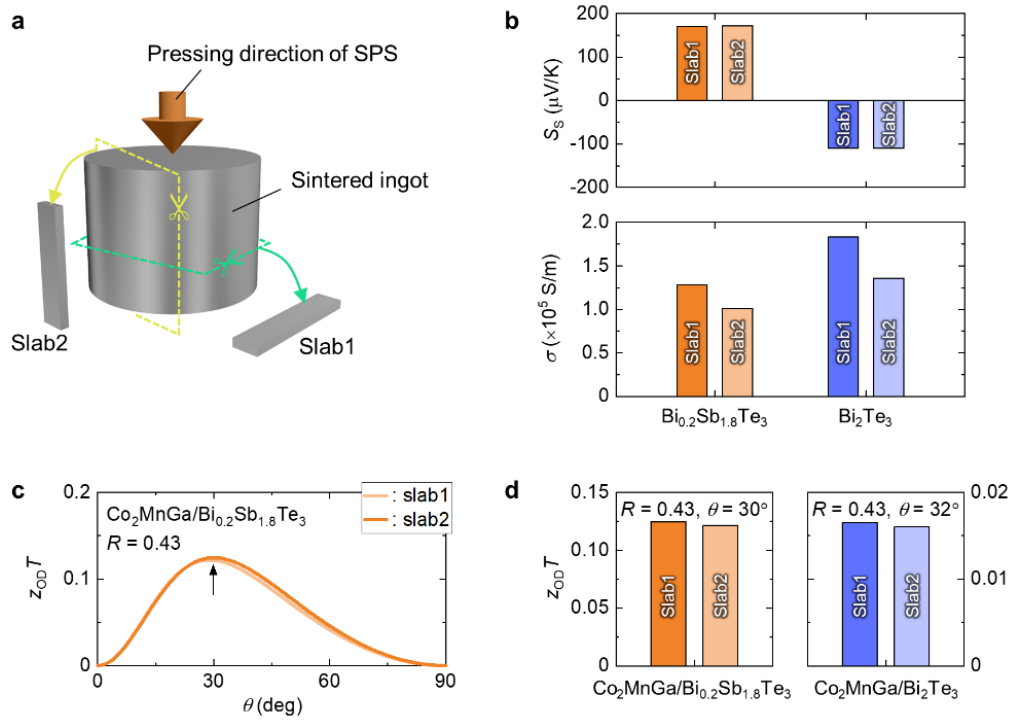
Supplementary Fig. 5 | Contribution of transverse magneto-thermoelectric effects in $\text{Co}_2\text{MnGa}/\text{Bi}_2\text{Te}_3$ ATML in cross-section configuration. **a,b** H -odd-dependent component of the lock-in amplitude A_{odd} (**a**) and phase ϕ_{odd} (**b**) images at $\mu_0|H| = 0.8$ T and $f = 10.0$ and 0.2 Hz in $\text{Co}_2\text{MnGa}/\text{Bi}_2\text{Te}_3$ ATML. Here, the magnetic field \mathbf{H} with the magnitude of H was applied along the vertical direction (z axis in Supplementary Fig. 4a) of the sample and μ_0 is the vacuum permeability.



Supplementary Fig. 6 | Contribution of transverse magneto-thermoelectric effects in Co₂MnGa/Bi₂Te₃ ATML in top-side configuration. **a,b** A_{odd} (**a**) and ϕ_{odd} (**b**) images at $\mu_0|H| = 0.8$ T and $f = 10.0$ and 0.2 Hz in Co₂MnGa/Bi₂Te₃ ATML. Here, **H** was applied along the horizontal short direction of the sample (y axis in Supplementary Fig. 4i). **c,d** $|H|$ dependence of A_{odd} (**c**) and ϕ_{odd} (**d**) at $f = 10.0$ Hz. Solid lines represent the results of linear fitting. **e,f** f dependence of A_{odd} (**e**) and ϕ_{odd} (**f**) at $\mu_0|H| = 0.8$ T. The data points in **c-f** were obtained by averaging the temperature modulation signal in the area defined by the green and blue rectangles in **a** and **b** for the Co₂MnGa and Bi₂Te₃ areas, respectively.



Supplementary Fig. 7 | Simulation of dimensionless figure of merit for transverse thermoelectric generation with hybridized ODSE and ANE in ATML. **a** Dependence of the absolute value of \tilde{S}_N on the magneto-thermoelectric modulation of the dimensionless figure of merit for hybrid transverse magneto-thermoelectric conversion $z_T T$, i.e., $\Delta(z_T T) = \tilde{S}_N^2 + 2|S_{\text{OD}}\tilde{S}_N|$, at various $|S_{\text{OD}}|$ values, where \tilde{S}_N is the effective anomalous Nernst coefficient in ATML [see Equation (4) in the main text]. **b** Contour maps of $z_T T$ as functions of $|\tilde{S}_N|$ and $|S_{\text{OD}}|$. Here, $\sigma_{xx} = 3.3 \times 10^5$ S/m and $\kappa_{yy} = 3.7$ W/mK obtained for Co₂MnGa/Bi_{0.2}Sb_{1.8}Te₃ ATML were used for estimating $\Delta(z_T T)$ and $z_T T$.



Supplementary Fig. 8 | Dependence of electrical and thermoelectric transport properties of sintered $\text{Bi}_{0.2}\text{Sb}_{1.8}\text{Te}_3$ and Bi_2Te_3 on pressing direction. **a** Schematic of the preparation of $\text{Bi}_{0.2}\text{Sb}_{1.8}\text{Te}_3$ and Bi_2Te_3 slabs. **b** S_s and σ of Slabs 1 and 2 for $\text{Bi}_{0.2}\text{Sb}_{1.8}\text{Te}_3$ and Bi_2Te_3 . **c** θ dependence of simulated $z_{\text{OD}}T$ for $\text{Co}_2\text{MnGa}/\text{Bi}_{0.2}\text{Sb}_{1.8}\text{Te}_3$ ATML at $R = 0.43$. The black arrow shows $z_{\text{OD}}T$ at θ of our $\text{Co}_2\text{MnGa}/\text{Bi}_{0.2}\text{Sb}_{1.8}\text{Te}_3$ ATML ($= 30^\circ$). The calculated value of $z_{\text{OD}}T$ is not changed by the difference in transport properties between Slabs 1 and 2. **d** $z_{\text{OD}}T$ at $R = 0.43$ and $\theta = 30^\circ$ (32°) for $\text{Co}_2\text{MnGa}/\text{Bi}_{0.2}\text{Sb}_{1.8}\text{Te}_3$ ($\text{Co}_2\text{MnGa}/\text{Bi}_2\text{Te}_3$) ATML.

Supplementary References

1. Goldsmid, H. J. Application of the transverse thermoelectric effects. *J. Electron. Mater.* **40**, 1254-1259 (2011).
2. Ando, F. et al. Multifunctional composite magnet for practical transverse thermoelectrics. Preprint at <https://arxiv.org/abs/2402.18019> (2024).
3. Kim, D. H. et al. Influence of powder morphology on thermoelectric anisotropy of spark-plasma-sintered Bi-Te-based thermoelectric materials. *Acta Mater.* **59**, 405-411 (2011).